J. Fluid Mech. (2002), *vol.* 473, *pp.* 103–145.
DOI: 10.1017/S0022112002002458 Printed in the United Kingdom

On the influence of coherent structures upon interscale interactions in turbulent plane jets

By C. B. da SILVA† AND O. MÉTAIS

LEGI-MOST/Institut de Mécanique de Grenoble, BP 53, 38041 Grenoble Cedex 09, France

(Received 17 April 2001 and in revised form 2 July 2002)

The influence of the coherent structures on grid/subgrid-scale (GS/SGS) interactions in free shear layers is analysed through the application of a top-hat filter to several plane jet direct numerical simulations (DNS). The Reynolds number based on the plane jet inlet slot width is $Re_h = 3000$. The study deals with energy containing (Kelvin–Helmholtz) and inertial range (streamwise) vortices, from the far field of the turbulent plane jet. The most intense kinetic energy exchanges between GS and SGS occur near these structures and not randomly in the space. The GS kinetic energy is dominated by GS advection and GS pressure/velocity interactions which appear located next to the Kelvin–Helmholtz rollers. Surprisingly, GS/SGS transfer is not very well correlated with the coherent vortices and GS/SGS diffusion plays an important role in the local dynamics of both GS and SGS kinetic energy. The so-called 'local equilibrium assumption' holds globally but not locally as most viscous dissipation of SGS kinetic energy takes place within the vortex cores whereas forward and backward GS/SGS transfer occurs at quite different locations. Finally, it was shown that SGS kinetic energy advection may be locally large as compared to the other terms of the SGS kinetic energy transport equation.

1. Introduction

The relation and interplay between large and small scales has long been one of the key problems of turbulence, and one that has received a considerable amount of attention since Kolmogorov's pioneering work (Kolmogorov 1941). Implicit in Kolmogorov's 'small scales universality' hypothesis, is the idea of a certain degree of large/small scales independence at sufficiently high Reynolds numbers. These ideas have become one of the building blocks of turbulence theory and have been used ever since, either to understand or model turbulent flows. However, in the last two decades, several theoretical, experimental and numerical studies have shown that large and small turbulent scales do not always behave independently, even in high-Reynolds-number flows. This is a key issue for the large-eddy simulation (LES) approach which depends heavily on a correct representation of large/small scale relationships. Indeed, in LES only the grid scales (GS) of motion are explicitly calculated and, since the subgrid-scales (SGS) are not computed, their effect on the resolved scales has to be adequately modelled through a proper SGS model. The reader is referred to the review articles by Lesieur & Métais (1996) and Meneveau & Katz (2000) for the recent SGS model developments and improvements. As frequently pointed out (see e.g. Piomelli & Chasnov 1996), the most important aspect the SGS model must represent accurately

† Present address: DEMEGI, Faculdade de Engenharía da Universidade de Porto, Rua Dr Roberto Frias, S/n 4200-465 Porto, Portugal. email: cbsilva@fe.up.pt

is the kinetic energy exchange between the resolved and unresolved scales. Although in the mean, the energy is predominantly transferred from GS to SGS (forward scatter), energy may also flow locally from SGS to GS (backward scatter). In some flow regions such as the buffer region in near wall flows or in the initial stages of transitional flows, backscatter can be more important than forward scatter (Piomelli *et al.* 1991; Piomelli, Yu & Adrian 1996; Hartel & Kleiser 1998). In this context, several works have been devoted to the study of large/small scale interactions and energy transfers (see e.g. Domaradzki & Rogallo 1990; Domaradzki, Liu & Brachet 1993; Domaradzki *et al.* 1994; Kerr, Domaradzki & Barbier 1996).

Another aspect that is beginning to receive increased attention is the effect and relation of coherent structures on GS/SGS interactions. Coherent structures arise naturally in many turbulent flows and it has been argued for a long time that they govern most of the energy of the turbulent flow and are responsible for most of the transfers of mass and momentum, whence their key role in turbulence. Much work concerning coherent structures and local turbulence dynamics was carried out by Hussain (1983, 1986) but only recently have the first studies on the role of coherent structures in GS/SGS interactions appeared. Piomelli *et al.* (1996) analysed the correlation of typical events from wall flows (sweeps and ejections) and GS/SGS transfer. For instance, in the buffer layer, forward scatter is associated with ejections, backward scatter with sweeps. Since upward and downward fluid motions are connected with streamwise vortices existing in the buffer layer, a strong correlation exists between these coherent structures and regions of positive/negative GS/SGS transfer. Regions of forward transfer are located in the upwash side of a streamwise vortex leg, backward transfer appears in the downwash region. Lin (1999) used LES to analyse the same phenomena in a planetary convective boundary layer, arriving at similar conclusions. Jiménez (1999) explained how the presence of vortices of different sizes at different wall locations, could promote a mechanism of backward energy cascade. In a series of articles, Horiuti (1995, 1996, 1997) studied in great detail the phenomena of spatial correlation between forward/backward scatter and coherent vortices in a mixing layer. He observed that the 'SGS production', taking place in the streamwise vortices, is positive (forward cascade) in the regions corresponding to the first and third quadrants of the rib vortices and negative (backward cascade) in the second and fourth quadrants. This was explained by the particular field of deformation rate caused by these streamwise structures. Horiuti (2000) analysed the types of vortical structure which are mostly responsible for the forward and backward cascade, in homogeneous isotropic turbulence. He saw that forward scatter primarily occurs along the flat sheet region, similar to the Burgers vortex layer, whereas the backward cascade mainly arises in the vortex tube core regions. Using turbulent wake laboratory experiments, O'Neil & Meneveau (1997) observed a strong influence between the von Kármán-street vortices and the so-called 'surrogate' ($\tau_{11}S_{11}^{<}$) subgrid-scale dissipation. The higher values of this quantity always appear ahead of the big rollers. The results of this study put in question the hypothesis of small scales universality, since the observed strong correlation between large and much smaller scales implies the existence of some level of anisotropy at small scales. This point was previously suggested by Piomelli, Coleman & Kim (1997) and Liu, Katz & Meneveau (1999) who studied the evolution of the subgrid-scales in non equilibrium turbulent flows. They showed that although it is true that subgrid-scales are more isotropic and adjust more rapidly from non-equilibrium situations than the large scales (Piomelli *et al.* 1997), they can be highly anisotropic and require a finite time to adjust themselves from external (large scale) effects. Recently, some attention was given to the influence

of SGS models on computed coherent structures. Silvestrini (1996) compared the coherent structures computed from a DNS of a mixing layer with those resulting from several SGS models. Vreman, Geurts & Kuerten (1997) observed that LES, made with different SGS models lead to differences in the vortical structures of a mixing layer. In a temporal plane jet DNS, Akhavan *et al.* (2000) noticed that different SGS models result in a different spatial structure of the subgrid-scale dissipation. They also observed intense regions of forward and backward transfer at the periphery of the flow vortical structures. Finally, Horiuti (1997, 2000) compared the topological performance of several SGS models in the streamwise vortices from a mixing layer and in the vortical structures from homogeneous isotropic turbulence (worms).

The present study is focused on understanding the effect of coherent structures upon GS/SGS interactions. For that purpose, three plane jet DNSs were carried out in which a box or top-hat filter was used to separate GS and SGS. Each term of the transport equations for the GS and SGS kinetic energy was analysed both statistically and topologically, in relation to the flow coherent structures. The several tools used in this study run from one-point statistics, including correlation coefficients, probability and joint probability density functions, to visualization of the instantaneous fields. In the end, new light is cast on how GS and SGS interact and what is the role played in it by the flow coherent vortices. Notice that the work is restricted to a local (in the physical space) analysis, since local interactions account for most of the GS/SGS transfers (Domaradzki & Rogallo 1990; Domaradzki *et al.* 1993, 1994). Moreover, this analysis is focused on relatively big coherent vortices, caused by a strong mean velocity field inhomogeneity and which are therefore quite different from the structures (worms) found in homogeneous isotropic turbulence.

Plane jets were chosen for the present study because they exhibit typical and well-documented events such as the development of Kelvin–Helmholtz vortices, streamwise or longitudinal vortex pairs, and vortex pairing/merging events. Since this kind of structure is not ubiquitous to plane jets, the conclusions from the present work can be extended to a large class of free shear flows. Recently, some well-resolved numerical simulations dealing with plane jets have been performed. Stanley, Sarkar & Mellado (2002) studied the mixing of a passive scalar in a direct numerical simulation of a spatially evolving plane jet. Le Ribault, Sarkar & Stanley (1999) made large-eddy simulations in order to assess (*a posteriori*) the performance of several turbulence models. Finally, Akhavan *et al.* (2000) used direct and large-eddy simulations of temporally evolving plane jets to analyse GS/SGS interactions in the physical and spectral space. Their study led them to the design of a new SGS model.

The organization of the paper is as follows. In the next section, the formalism of the LES and the transport equations for both the GS and SGS kinetic energy are recalled. In §3, the numerical method, physical and computational parameters of the DNS are detailed. In §4, the present DNS is thoroughly validated by comparisons with previous experimental data and numerical simulations. Section 5 uses the far-field region of the present DNS to analyse in detail how the presence of strong coherent vortices affects both the statistical and local GS/SGS interactions.

2. Problem formulation

2.1. *Governing equations*

2.1.1. *Filtered Navier–Stokes equations*

In LES, all the existing scales of motion are decomposed into a grid scale ($f^<$) and a subgrid-scale part ($f^>$) through a spatial filtering operator applied to the

Navier–Stokes (NS) equations. The filtering operator is defined by

$$f^{<}(x) = \int_{\Omega} f(x')G_{\Delta}(x - x')\,\mathrm{d}x, \tag{2.1}$$

where $G_{\Delta}(x)$ is a filter of width Δ, $f(x)$ represents any flow variable and the integration is carried out over the whole flow domain, Ω. Therefore, the velocity and pressure fields can be decomposed as

$$u_i = u_i^{<} + u_i^{>}, \quad p = p^{<} + p^{>}, \tag{2.2}$$

respectively.

It is important to realize that the filter function has to verify,

$$\int_{\Omega} G_{\Delta}(x)\,\mathrm{d}x = 1, \tag{2.3}$$

in the analytical and computational (discrete) sense. The resulting filtered Navier–Stokes equations are then,

$$\frac{Du_i^{<}}{Dt} = \frac{\partial u_i^{<}}{\partial t} + \frac{\partial u_i^{<}u_j^{<}}{\partial x_j} = -\frac{\partial p^{<}}{\partial x_i} + \nu\frac{\partial}{\partial x_j}\left(\frac{\partial u_i^{<}}{\partial x_j} + \frac{\partial u_j^{<}}{\partial x_i}\right) - \frac{\partial \tau_{ij}}{\partial x_j}, \tag{2.4}$$

$$\frac{\partial u_i^{<}}{\partial x_i} = 0. \tag{2.5}$$

Here, $p^{<}$ means $p^{<}/\rho$ for convenience. τ_{ij} is the unknown subgrid-stress tensor responsible for the momentum exchanges between the subgrid and the filtered scales and which has to be modelled:

$$\tau_{ij} = (u_i u_j)^{<} - u_i^{<}u_j^{<}. \tag{2.6}$$

Throughout this paper, angle brackets, $\langle\ \rangle$, will be used to designate mean quantities whereas fluctuating quantities will be marked with a prime. With this notation, any instantaneous variable v can be Reynolds decomposed as $v = \langle v\rangle + v'$. Details about the sample data sets and averaging procedures will be given in each section.

2.1.2. *Transport equations for the grid-scale and subgrid-scale kinetic energy*

A first step to understanding the interaction between grid scales (GS) and subgrid-scales (SGS) consists of writing out the transport equations for (twice) the total GS and SGS kinetic energy. This was previously done by Piomelli & Chasnov (1996), Piomelli *et al.* (1991, 1996).

The transport equation for (twice) the GS kinetic energy, $u_i^{<}u_i^{<}$, is given by,

$$\underbrace{\frac{\partial u_i^{<}u_i^{<}}{\partial t}}_{\mathrm{I}} + \underbrace{\frac{\partial u_i^{<}u_i^{<}u_k^{<}}{\partial x_k}}_{\mathrm{II}} = \underbrace{-2\frac{\partial}{\partial x_k}(p^{<}u_k^{<})}_{\mathrm{III}} + \underbrace{\frac{\partial}{\partial x_k}\left(\nu\frac{\partial}{\partial x_k}(u_i^{<}u_i^{<})\right)}_{\mathrm{IV}} - \underbrace{2\nu\frac{\partial u_i^{<}}{\partial x_k}\frac{\partial u_i^{<}}{\partial x_k}}_{\mathrm{V}} - \underbrace{2\frac{\partial}{\partial x_k}(\tau_{ik}u_i^{<})}_{\mathrm{VI}} + \underbrace{2\tau_{ik}S_{ik}^{<}}_{\mathrm{VII}}, \tag{2.7}$$

and the transport equation for the SGS kinetic energy, τ_{ii} is,

$$\underbrace{\frac{\partial \tau_{ii}}{\partial t}}_{\text{VIII}} + \underbrace{\frac{\partial (\tau_{ii} u_k^<)}{\partial x_k}}_{\text{IX}} = \underbrace{\frac{\partial}{\partial x_k}\left((u_i u_i)^< u_k^< - (u_i u_i u_k)^<\right)}_{\text{X}} + 2\underbrace{\frac{\partial}{\partial x_k}\left(p^< u_k^< - (p u_k)^<\right)}_{\text{XI}}$$
$$+ \underbrace{\frac{\partial}{\partial x_k}\left(\nu \frac{\partial}{\partial x_k} \tau_{ii}\right)}_{\text{XII}} - 2\nu \underbrace{\left(\left(\frac{\partial u_i}{\partial x_k}\frac{\partial u_i}{\partial x_k}\right)^< - \frac{\partial u_i^<}{\partial x_k}\frac{\partial u_i^<}{\partial x_k}\right)}_{\text{XIII}}$$
$$+ 2\underbrace{\frac{\partial}{\partial x_k}(\tau_{ik} u_i^<)}_{\text{XIV}} - 2\underbrace{\tau_{ik} S_{ik}^<}_{\text{XV}}, \tag{2.8}$$

here, $S_{ij}^< = \frac{1}{2}((\partial u_i^</\partial x_j) + (\partial u_j^</\partial x_i))$ is the GS deformation tensor. It is important to recall the physical meaning of these equations. In (2.7), terms I and II account for the total (local and convective) variation of GS kinetic energy. Terms III and IV account for the redistribution (diffusion) of GS kinetic energy by pressure/velocity interactions and molecular viscosity, respectively. Term V is the local GS kinetic energy dissipation due to the molecular viscosity. The terms VI and VII are the only terms involving the subgrid-stress tensor τ_{ij} and are directly related to the kinetic energy exchanges between GS and SGS. Term VI (GS/SGS diffusion) represents a redistribution of GS kinetic energy by interactions between the GS velocity and the SGS stresses. The GS/SGS transfer (term VII),

$$T_{sgs}^< = 2\tau_{ik} S_{ik}^<, \tag{2.9}$$

also called subgrid-scale dissipation, is thought to be the dominating term in the equation. It represents the transfer of kinetic energy between GS and SGS. If $T_{sgs} < 0$, the term is a sink for the GS kinetic energy as energy flows from GS to SGS (forward scatter). If $T_{sgs} > 0$, term VII is a source and the kinetic energy flows from SGS to GS (backward scatter).

In (2.8), terms VIII and IX represent the local and convective variation of the SGS kinetic energy, respectively. The diffusion caused by the local turbulence level on the SGS kinetic energy is represented by term X (SGS turbulent transport). Term XI is the SGS pressure/velocity interactions and XII is the SGS viscous diffusion. Term XIII (SGS viscous dissipation) represents the end of the energy cascade process where molecular viscosity finally dissipates the remaining SGS kinetic energy.

It is important to notice that the terms XIV and XV are, respectively, the opposites of the terms VI and VII. Since these terms appear in both equations with opposite signs, they represent the kinetic energy exchange between GS and SGS. As stressed above, the terms VI and VII involve the subgrid-scale stress tensor and an inaccurate modelling of these two terms will yield an incorrect representation of the energetic exchanges between GS and SGS.

3. Numerical method and DNS parameters

3.1. *Spatial and temporal discretization*

The code used here is a highly accurate spectral/compact finite-difference incompressible Navier–Stokes solver. The discretization of the spatial derivatives was done using a sixth-order-compact scheme (Lele 1992) in the streamwise (x) direction and

pseudospectral methods (Canuto *et al.* 1987) for the normal (y) and spanwise (z) directions.

The time advancement uses an explicit three-step third-order low-storage Runge–Kutta time-stepping scheme (Williamson 1980). Pressure velocity coupling is solved with a fractional step method (Kim & Moin 1985; Le & Moin 1991) that ensures incompressibility at each substep of the Runge–Kutta time-advancing scheme.

3.2. *Boundary conditions*

Since we are here dealing with spatially growing flows, special care has to be taken of the inflow and outflow boundary conditions (streamwise, x-direction). In particular, we must be sure that the coherent structures exit the computational domain properly without being affected by the outflow boundary condition. For this purpose, the code uses a non-reflective (Orlansky 1976) outflow condition in which not only the convective but also the viscous terms of the Navier–Stokes equations are explicitly advanced (Gonze 1993). It was previously checked by Comte, Silvestrini & Begou (1998) in DNS and LES of spatially growing mixing layers that the coherent structures leave the computational domain without being distorted. The boundaries in the normal (y) direction were taken as periodic. Such boundary conditions, which permit the use of very accurate pseudospectral schemes, do not allow entrainment from the flow situated outside the computational domain. However, it has been clearly shown by Stanley, Sarkar & Mellado (2002) and Stanley & Sarkar (2000) that the imposition of a small co-flow allows us to obtain a very good statistical concordance with experimental measurements as long as the lateral boundary conditions of the jet are placed sufficiently far away. As subsequently demonstrated, our results are carefully validated by comparing with experimental measurements (Gutmark & Wygnansky 1976; Browne *et al.* 1983; Ramprian & Chandrasekhara 1985; Thomas & Chu 1989; Thomas & Prakash 1991), and other DNS (Le Ribault *et al.* 1999; Stanley & Sarkar 2000; Stanley *et al.* 2002). Finally, the spanwise (z) direction was treated as periodic.

3.3. *Inflow conditions*

A velocity profile is prescribed at the inlet at each time step. The mean inlet velocity is based in a hyperbolic tangent profile (Le Ribault *et al.* 1999; Stanley *et al.* 2002),

$$U = \frac{U_1 + U_2}{2} + \frac{U_1 - U_2}{2} \tanh\left(\frac{h}{2\theta_0}\frac{y_{sl}}{h}\right). \tag{3.1}$$

Here, U_1 is the jet centreline velocity and U_2 is a small co-flow. The mean V and W velocities in the y- and z-directions were set to zero at the inlet. θ_0 is the momentum thickness of the initial shear layer, h is the jet's inlet slot width, and y_{sl} is the distance from the centre of the shear layer. Notice that (3.1) has to be mirrored about the plane (x, z) in order to obtain the desired jet top-hat profile. The inlet profile expressed in a reference frame placed at the centre of the jet ($y = 0$) is then given by,

$$U(x = 0, y, z) = \frac{U_1 + U_2}{2} + \frac{U_1 - U_2}{2} \tanh\left[\frac{h}{4\theta_0}\left(1 - \frac{2|y|}{h}\right)\right]. \tag{3.2}$$

A three-component (u, v and w) fluctuating velocity field was superimposed on the mean velocity profile. This numerical noise was designed to exhibit the statistical characteristics of isotropic turbulence. Each velocity component of the noise is prescribed in such a way that its energy spectrum is given by

$$E(k) \propto k^s \exp[-\tfrac{1}{2}s(k/k_0)^2] \tag{3.3}$$

where $k = (k_y^2 + k_z^2)^{1/2}$ is the wavenumber norm in the (y, z)-plane and the exponent s and the peak wavenumber k_0 were chosen to give an energy input dominant at small scales (high k_0) and an energy content typical of freely decaying turbulence ($s \leqslant 4$). The noise was only imposed within the shear-layer region of the mean profile through a proper convolution function.

3.4. *Computational parameters of the DNS*

In this work, we will be interested mainly in analysing grid/subgrid-scale interactions in a fully developed turbulent configuration. For this purpose, we used the same strategy as Stanley & Sarkar (2000) and Stanley *et al.* (2002) which consists of applying a relatively high-amplitude inlet noise in order to force the flow to reach the self-similar state quickly (earlier than in other numerical simulations carried out at the same Reynolds number). This in turn allows the validation of the present simulations through comparisons with experimental data taken from the self-similar regime at higher Reynolds numbers. The influence of the inlet noise amplitude in direct numerical simulations of spatially developing plane jets was investigated by Stanley & Sarkar (2000). They concluded that 'the influence of the forcing is rapidly lost downstream' and the effects of applying a high-amplitude noise (10%) are only felt in the near field ($x/h < 4$) and do not influence the jet dynamics in the self-similar region. To show that our main results are independent of the inlet noise we vary its level by considering both 5% and 10% noise amplitudes.

Three DNSs of plane jets are carried out here. In the first simulation (DNS0) the initial shear-layer momentum thickness θ_0 non-dimensionalized by the inlet slot width h was set to $h/\theta_0 = 30$ and the maximum intensity of the inlet velocity fluctuations is 5% of the maximum inlet velocity, U_1. The second simulation (DNS1) uses the same parameters as Stanley *et al.* (2002) in which $h/\theta_0 = 20$ and the magnitude of the inlet velocity fluctuations is set to $10\%U_1$. Finally, the third simulation (DNS2) uses the same noise intensity as in DNS1 but the ratio h/θ_0 is raised to 30 as in DNS0. As will be shown below, all simulations have a quick transition to turbulence and reach the self-similar state before the end of the computational domain. The Reynolds number was $Re_h = \Delta U h/\nu = 3000$ for all three simulations, where $\Delta U = U_1 - U_2$ are the maximum and minimum (co-flow) jet velocities which were set to $U_1 = 1.091$ and $U_2 = 0.091$, respectively. Our co-flow has a similar magnitude ($U_2/U_1 \approx 0.08$) as that used by Le Ribault *et al.* (1999), Stanley & Sarkar (2000) and Stanley *et al.* (2002). In these previous studies, it was demonstrated that such a small co-flow has only a minor influence on the jet dynamics. The same is true in the present case, as will be shown below.

Table 1 summarizes the computational parameters for the three simulations. The total number of grid points is equal to about 6.7 (DNS0, DNS1) and 7.4 (DNS2) million. Notice that the grid is uniform in the three spatial directions with $\Delta x = \Delta y = \Delta z = 0.04h$.

3.5. *Filtering procedure*

This work is aimed at the study of the local interactions between large and small scales, thus only a spatially localized filter can be used (Liu, Meneveau & Katz 1994). Here, we use a box or top-hat filter defined as

$$G_\Delta(\boldsymbol{x} - \boldsymbol{\xi}) = \begin{cases} 1/\Delta & \text{if } |\boldsymbol{x} - \boldsymbol{\xi}| < \frac{1}{2}\Delta \\ 0 & \text{otherwise.} \end{cases}.$$

Simulation	h/θ	Noise (%)	$(n1 \times n2 \times n3)$	$(L_x \times L_y \times L_z)$	Resolution
DNS0	30	5	$(310 \times 300 \times 72)$	$(12.4h \times 12h \times 2.9h)$	$\Delta x_i = 0.04h$
DNS1	20	10	$(310 \times 300 \times 72)$	$(12.4h \times 12h \times 2.9h)$	$\Delta x_i = 0.04h$
DNS2	30	10	$(310 \times 300 \times 80)$	$(12.4h \times 12h \times 3.2h)$	$\Delta x_i = 0.04h$

TABLE 1. Summary of the physical and computational parameters for the three DNS, used in this work. Notice that the grid is uniform in the three spatial directions and $\Delta x_i = \Delta x = \Delta y = \Delta z$. $n1$, $n2$ and $n3$ are the number of grid points in the x (streamwise), y (normal) and z (spanwise) directions, respectively, and L_x, L_y and L_z the dimensions of the computational domain along the three space directions.

As pointed out by Meneveau & Katz (2000), using such a filter, in the subgrid-scales kinetic energy, there is a dominant contribution from the small scales, but also a smaller contribution from the grid scales, and vice versa for the grid-scale kinetic energy. However, we use a box filter because it corresponds to the filter implicitly associated with the discretization in a centred second-order finite difference (Rogallo & Moin 1984) or finite volume (Schumann 1975) code, which is often used in large-eddy simulations. Furthermore, we have checked that the use of a Gaussian filter leads to similar results. To analyse the influence of the filter width, we use two different box filters with $\Delta_1 = 3\Delta x$ and $\Delta_2 = 5\Delta x$.

4. DNS assessment

4.1. *Coherent structures*

In this subsection, our DNS results will be used to validate the code in the plane jet configuration. As stressed before, all three simulated flows reach the self-similar state, which makes possible the comparison of the present results with several experimental measurements, usually carried out at much higher Reynolds numbers.

An idea of the general three-dimensional organization of the three plane jet DNSs can be gained from figure 1. The figure shows top-view isosurfaces of positive Q criteria (Hunt, Wray & Moin 1988), which is the second invariant of the velocity gradient tensor, $Q = (1/2)(\Omega_{ij}\Omega_{ij} - S_{ij}S_{ij})$ where Ω and S are its symmetric and anti-symmetric parts, respectively. The positive Q has proved to be a good criterion to identify coherent vortices in various wall-bounded and free-shear flows (Dubief & Delcayre 2000). Side-view isosurfaces of high vorticity modulus for simulation DNS2 are shown in figure 2. DNS0 and DNS1 show similar trends.

The vorticity isosurfaces showed that for the three DNSs, the flow appears to be smooth in the early stages of transition until the appearance of the first pair of Kelvin–Helmholtz vortices, both at the upper and lower shear layers. They appear at $x/h \approx 3.2$, $x/h \approx 3.5$ and $x/h \approx 3$ for simulations DNS0, DNS1 and DNS2, respectively. Comparing simulations DNS0 (5% noise, $h/\theta_0 = 30$) and DNS2 (10% noise, $h/\theta_0 = 30$), we see that the transition in DNS2 is quicker owing to its higher values of inlet noise. Similarly, comparing DNS1 (10% noise, $h/\theta_0 = 20$) and DNS2 (10% noise, $h/\theta_0 = 30$), we see that the smaller initial momentum thickness in DNS2 accelerates its transition stage. Thus, an increase of either the ratio h/θ_0 or the inlet noise, causes a faster transition to turbulence. This agrees with the findings of Stanley & Sarkar (2000) who analysed the effect of the initial values of h/θ_0 and of the amplitude noise in several DNSs of plane jets. However, the coherent structures

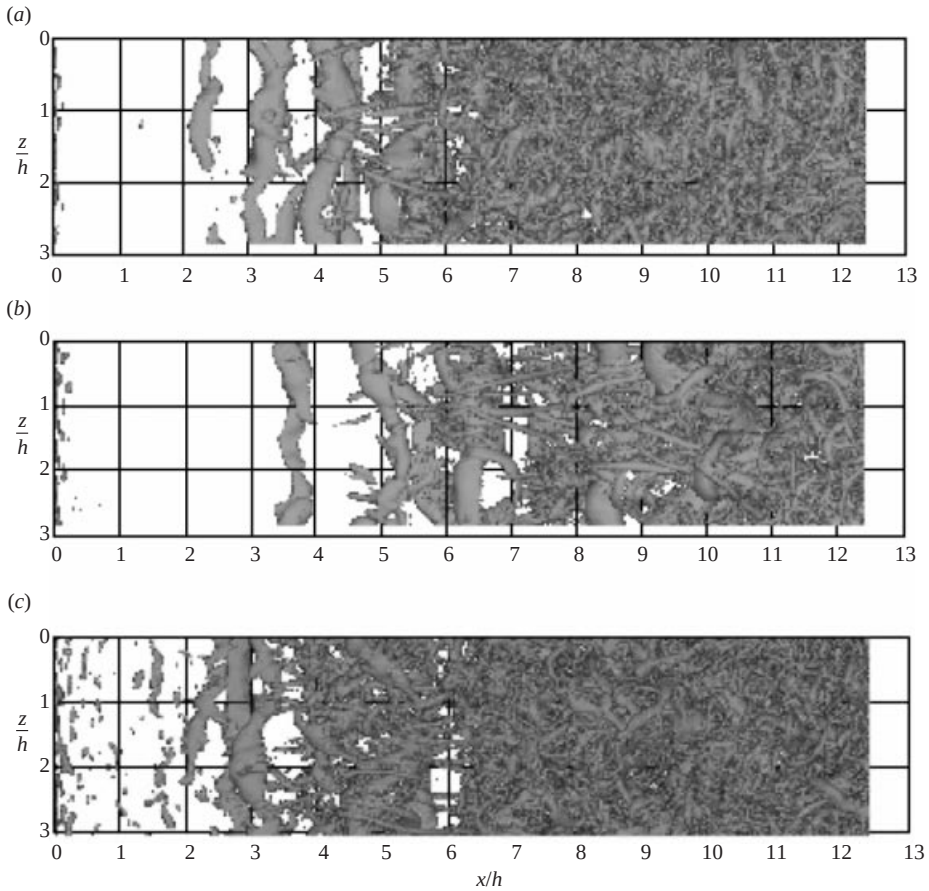

FIGURE 1. Top view of positive Q criteria for the three DNSs: (a) DNS0; (b) DNS1; (c) DNS2. In all three cases the threshold chosen is $4.0(U_1/h)^2$ and Q varies between $Q_{min} = -484(U_1/h)^2$ and $Q_{max} = +1082(U_1/h)^2$ for DNS0, $Q_{min} = -399(U_1/h)^2$ and $Q_{max} = +968(U_1/h)^2$ for DNS1 and $Q_{min} = -856(U_1/h)^2$ and $Q_{max} = +1189(U_1/h)^2$ for DNS2.

found in the three cases remain similar, as can be checked in figure 1. As shown in figure 2, in agreement with Thomas & Goldschmidt (1986), for a near top-hat plane-jet initial-velocity profile, the upper and lower primary Kelvin–Helmholtz vortices appear symmetrically arranged with respect to the centreline (x, z)-plane showing the preferential amplification of the varicose mode. As did Thomas & Goldschmidt (1986), we notice an asymmetrical arrangement of the jet further downstream owing to the subsequent growth of a sinuous mode. The isosurfaces of the positive Q criterion (see figure 1) show that these initial Kelvin–Helmholtz vortices are significantly distorted along the spanwise direction. Further downstream, intense streamwise vortex pairs are seen to emerge and to connect each two consecutive Kelvin–Helmholtz billows. Most of the vorticity modulus is concentrated in these secondary structures, which start to be visible, through isosurfaces of vorticity modulus, when the threshold reaches about 44% of its maximum value.

To give a greater insight into the coherent structures present in the far-field region of the plane jet, figures 3 and 4 show details of the region $5.5 < x/h < 12.4$ for DNS1 and DNS2, respectivley. For clarity, only the upper shear layer ($y/h > 0$) is

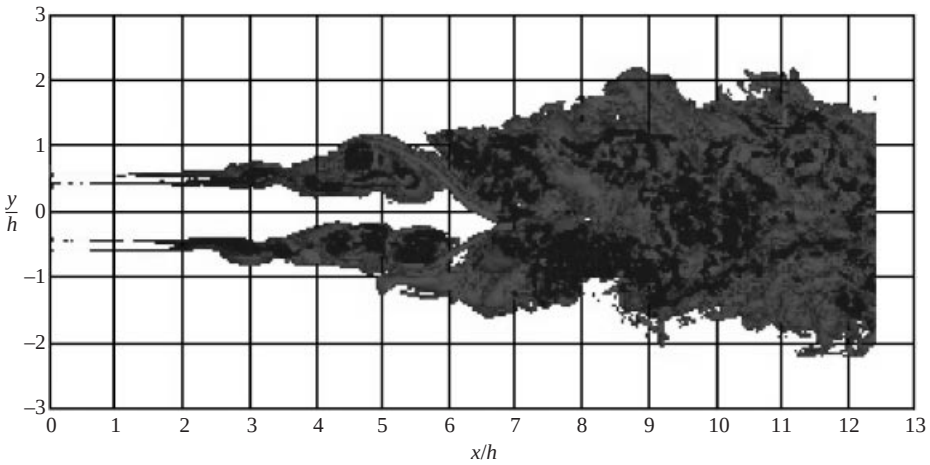

FIGURE 2. Side view of the vorticity modulus Ω, for DNS2. The threshold chosen is $6.23(U_1/h)$ and Ω varies between $\Omega_{min} = 0(U_1/h)$ and $\Omega_{max} = +72.63(U_1/h)$. Notice that the full extent of the lateral domain is $12h$ while these figures show only the region $-3 < y/h < +3$.

shown. Pressure isosurfaces for simulations DNS1 and DNS2 are shown in figures 3(a) and 4(a), whereas isosurfaces of the positive Q criterion are shown in figures 3(b) and 4(b), respectively. For DNS1, two large Kelvin–Helmholtz vortices situated around $x/h \approx 6.2$ and $x/h \approx 8.5$ are clearly identified through the low-pressure isosurfaces (figure 3a). The vortex-identification criterion based upon Q involves much more small-scale activity than that based on the pressure as it is clear that the isobaric surfaces are fatter than the Q isosurfaces. Note that only the most intense vortices, either spanwise or streamwise, are visible through the pressure and that the Q criteria not only displays these intense structures but also provides a much more detailed view of the other small-scale structures. In particular, it can be seen that intense small-scale activity takes place within the core of the large Kelvin–Helmholtz vortices in the regions where the streamwise vortices connect with the latter (see figure 3b). Compared to DNS1, we can see that in DNS2 the coherent structures are now much more distorted and fragmented (see figure 4). However, we can still observe the presence of strong Kelvin–Helmholtz billows. One such roller is present at $x/h \approx 6.75$ (see figure 4a). In DNS2, the smaller coherent vortices never show clearly in the pressure isosurfaces owing to the high level of background turbulence. They are more easily evidenced using isosurfaces of the positive Q criterion (see figure 4b). In this simulation, for $x/h \gtrsim 6$, we observe that the coherent vortices have lost almost any preferential spatial orientation. This may be a sign of a locally isotropic turbulent state (see below). DNS0 (not shown) exhibited similar features.

4.2. *Statistics*

This section analyses one-point statistics from simulations DNS0/DNS1/DNS2 in order to validate the code in the plane-jet configuration. All the statistics shown in this section were calculated by accumulating data over 6000/7500/8000 run iterations (instantaneous fields) and along the spanwise direction (72/72/80 points). The total elapsed time allows for more than 28/35/38 Kelvin–Helmholtz vortices to leave the computational domain both at the upper and lower shear layers.

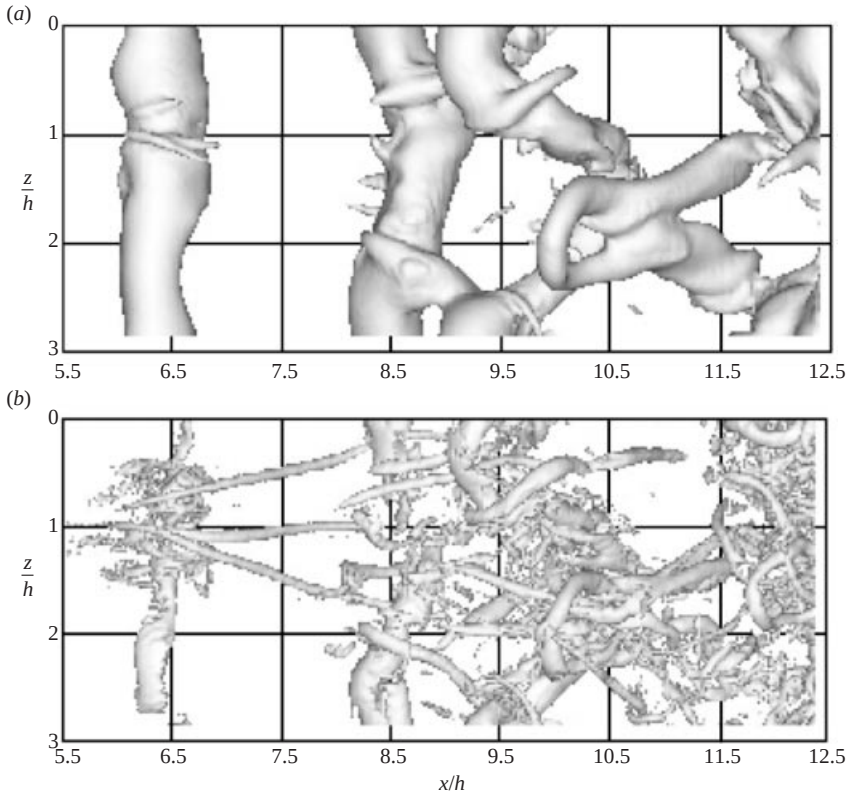

FIGURE 3. (*a*) Top-view isosurfaces of low pressure p in the upper shear layer ($y/h > 0$) for simulation DNS1. The threshold chosen is $-0.13\rho U_1^2$ and p varies between $p_{Min} = -0.6\rho U_1^2$ and $p_{max} = 0.27\rho U_1^2$; (*b*) Top-view isosurfaces of positive Q in the upper shear layer ($y/h > 0$) for simulation DNS1. The threshold chosen is $+14.23(U_1/h)^2$ and Q varies between $Q_{min} = -399(U_1/h)^2$ and $Q_{max} = +968(U_1/h)^2$. Both pictures show a subdomain of the simulation from $x/h = 5.5$ to $x/h = 12.4$ and the spanwise dimension is the total spanwise domain length, $L_z = 2.9h$. Both figures report the same instant which also corresponds to the instant of figure 1.

Figure 5(*a*) displays the streamwise evolution of the jet half-width, defined as the distance $\delta_U(x)$ for which,

$$\langle u(x, y = \delta_U(x))\rangle - U_{2L} = 0.5(U_C - U_{2L}). \tag{4.1}$$

$U_C = \langle u(x, y = 0)\rangle$ is the centreline mean velocity, $U_{2L} = \langle u(x, y = \infty)\rangle$ is the local co-flow velocity. At the inlet $U_{2L} = U_2$, where U_2 is the inlet co-flow velocity from (3.2). The centreline mean streamwise velocity is shown in figure 5(*b*). These results are compared with the DNS of Stanley *et al.* (2002) (same Reynolds number) and with the measured values from Browne *et al.* (1983) and Thomas & Chu (1989) (higher Reynolds numbers).

In the self-similar regime, plane jets obey the following linear relationships (Gutmark & Wygnansky 1976; Ramprian & Chandrasekhara 1985; Thomas & Chu 1989):

$$\frac{\delta_U}{h} = K_{u1}\left[\frac{x}{h} + K_{u2}\right], \tag{4.2}$$

$$\left[\frac{U_1 - U_2}{U_C - U_2}\right]^2 = C_{u1}\left[\frac{x}{h} + C_{u2}\right]. \tag{4.3}$$

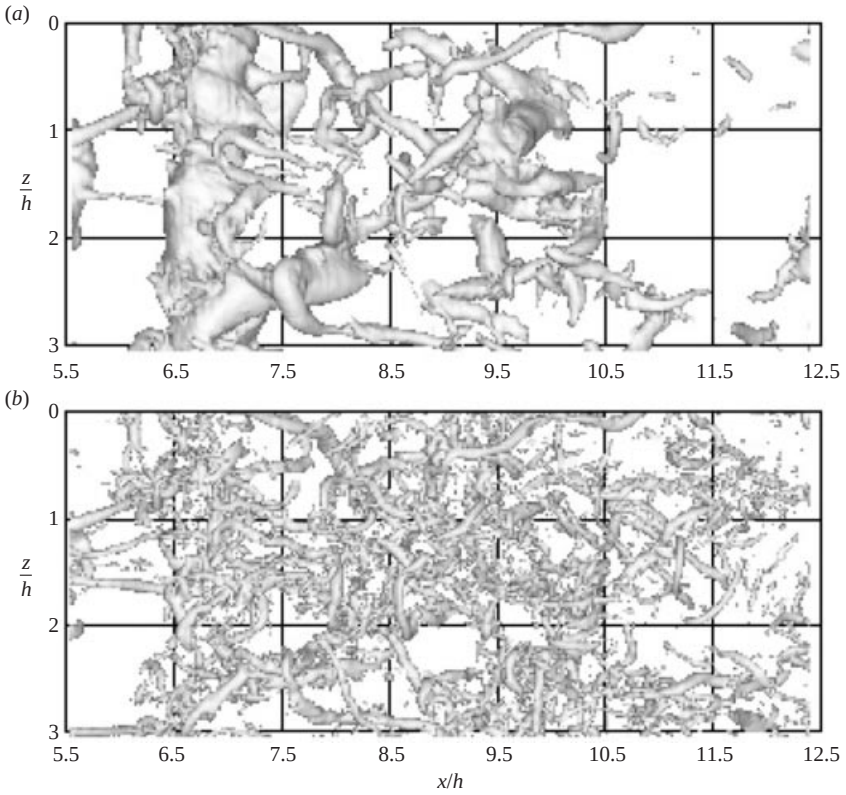

FIGURE 4. (*a*) Top-view isosurfaces of pressure p in the upper shear layer ($y/h > 0$) for simulation DNS2. The threshold chosen is $-0.12\rho U_1^2$ and p varies between $p_{min} = -0.57\rho U_1^2$ and $p_{max} = 0.16\rho U_1^2$; (*b*) Top-view isosurfaces of positive Q in the upper shear layer ($y/h > 0$) for simulation DNS2. The threshold chosen is $+31.77(U_1/h)^2$ and Q varies between $Q_{min} = -856(U_1/h)^2$ and $Q_{max} = +1189(U_1/h)^2$. Both pictures show a subdomain of the simulation from $x/h = 5.5$ to $x/h = 12.4$ and the spanwise dimension is the total spanwise domain length, $L_z = 3.2h$. Both figures report the same instant which also corresponds to the instant of figure 1.

Figure 5 shows also the straight lines for the self-similar region, corresponding (4.2) and (4.3) for all three simulations. The corresponding growth rates and centreline velocity decay coefficients are given in table 2 with the values obtained from several numerical and experimental studies.

These graphs show that all three simulations DNS0, DNS1 and DNS2 exhibit a linear evolution typical of the self-similar regime. As expected, and in agreement with the numerical simulations of Stanley & Sarkar (2000), the self-similar regime is attained earlier in DNS2 ($x/h > 7$) than in DNS1 ($x/h > 9$) or DNS0 ($x/h > 7.5$) owing to its higher initial noise and h/θ_0. Moreover, in the three simulations the slope of the half-width and centreline velocity decay agree very well with the available experimental and numerical data (see table 2 and also the decay coefficients found by Stanley & Sarkar 2000). We note, however, that the self-similar regime is attained faster in the experimental data, which correspond to higher Reynolds numbers, and in the numerical simulations of Stanley *et al.* (2002), at the same Reynolds number. It is well established that the plane jet is very sensitive to the inlet conditions (see e.g. Thomas & Chu 1989). Consequently, in the initial stages of transition, a perfect match for both the half-width growth and for the potential core length is very

Source	K_{1u}	K_{2u}	C_{1u}	C_{2u}
DNS0 results	0.089	+2.10	0.165	−0.85
DNS1 results	0.108	−2.10	0.20	−2.75
DNS2 results	0.089	+0.80	0.165	−0.25
DNS Stanley *et al.* (2002)	0.092	+2.62	0.201	+1.23
Ramparian & Chandrasekhara (1985)	0.110	−1.00	0.093	−1.60
Browne *et al.* (1983)	0.104	−5.00	0.143	−9.00
Thomas & Prakash (1991)	0.110	+0.14	0.220	−1.20
Thomas & Chu (1989)	0.110	+0.14	0.220	−1.19
Gutmark & Wygnansky (1976)	0.100	−2.00	0.189	−4.72
Hussain & Clark (1977)	0.118	+2.15	0.123	+4.47

TABLE 2. Growth rates and centreline velocity decay coefficients for the present simulations (DNS0, DNS1 and DNS2) and values obtained from other numerical simulations (Stanley *et al.* 2002) and experimental measurements (Gutmark & Wygnansky 1976; Hussain & Clark 1977; Browne *et al.* 1983; Ramprian & Chandrasekhara 1985; Thomas & Chu 1989; Thomas & Prakash 1991).

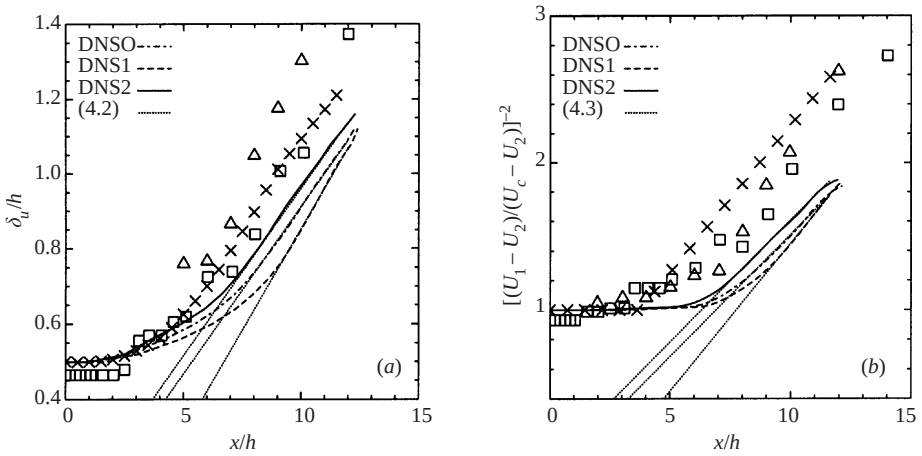

FIGURE 5. (*a*) Downstream evolution of the half-width for several plane jets; (*b*) Downstream evolution of the centreline velocity decay for several plane jets. The results from simulations DNS0, DNS1 and DNS2 are compared with the experimental data from △, Browne *et al.* (1983) and □, Thomas & Chu (1989), as well as the DNS from ×, Stanley *et al.* (2002). (*a*) Equation (4.2) has $K_{1u} = 0.089$ and $K_{2u} = +2.10$ for DNS0, $K_{1u} = 0.108$ and $K_{2u} = -2.10$ for DNS1, and $K_{1u} = 0.089$ and $K_{2u} = +0.80$ for DNS2. (*b*) Equation (4.3) has $C_{1u} = 0.165$ and $C_{2u} = -0.85$ for DNS0, $C_{1u} = 0.20$ and $C_{2u} = -2.75$ for DNS1 and $C_{1u} = 0.165$ and $C_{2u} = -0.25$ for DNS2.

difficult to obtain with distinct experimental apparatus or numerical simulations. The difference between the DNS1 results and the simulation of Stanley *et al.* (2002) can be explained by the fact that these authors force the inlet noise spectrum to peak at the fundamental mode for a hyperbolic tangent profile, whereas we apply a white noise peaking at small scales to let the fundamental frequency emerge naturally. Thus, our 'synthetic' noise yields a longer distance for the coherent structures to appear and a slower transition towards a turbulent state. The maximum amplitude noise used by Stanley *et al.* (2002) is also $10\%U_1$. Stanley & Sarkar (2000) analysed the effect of the initial values of h/θ_0 (11, 20 and 40) and of the amplitude noise (2.5%, 5% and 10%) in several DNSs of plane jets. They concluded that these initial differences lead to similar growth rates in the self-similar region and affect only the extent of

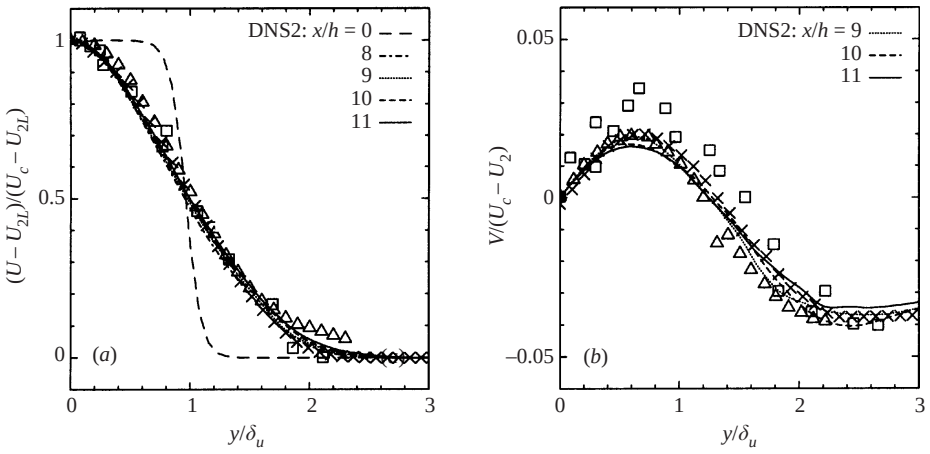

FIGURE 6. (*a*) Mean streamwise velocity profiles of the plane jet for several downstream positions. (*b*) Mean normal velocity profiles of the plane jet for several downstream positions. Both curves correspond to simulation DNS2 and are compared with the experimental data from △, Gutmark & Wygnansky (1976) and □, Ramprian & Chandrasekhara (1985), as well as the DNS from ×, Stanley *et al.* (2002) (at $x/h = 10.5$).

the potential core region. As can be seen in figure 5, the same is true in the present simulations. Note that the slopes corresponding to DNS0 and DNS2 (same h/θ_0) are equal to and slightly smaller than the slope corresponding to DNS1 (smaller h/θ_0). This agrees also with the results from Stanley & Sarkar (2000). Therefore, we can consider that our computations exhibit the correct self-similar behaviour and that the far field is representative of the fully developed turbulent regime.

The mean streamwise velocity profiles for DNS2 at several downstream locations are shown in figure 6(*a*). Self-similarity is observed for $x/h > 8$, as all the profiles in $8 < x/h < 11$ collapse. The results agree very well with both the previous DNS and experimental measurements. Figure 6(*b*) displays the mean normal velocity profiles for DNS2. Again, good agreement is observed between the present results and the previous numerical and experimental data. Note that the normal velocity is very sensitive to the nature of the lateral boundary conditions; figure 6(*b*) therefore demonstrates that our lateral boundaries were placed sufficiently far a way and do not affect the entrainment rate. Note that similar results are obtained with DNS0 and DNS1, although the self-similar regime is obtained later than in DNS2.

Figure 7(*a*) shows the streamwise Reynolds stresses profiles for simulation DNS2, at several downstream locations. Comparing the profiles at $x/h = 9$, $x/h = 10$ and $x/h = 11$ we can see that the Reynolds stresses are very close to the self-similar state. Considering the scatter between the experimental data, the present results (DNS2) agree well with the data available. The same is true of the lateral and spanwise Reynolds stresses profiles (not shown). The figure 7(*b*) displays the downstream evolution of the streamwise Reynolds stresses at the centreline. Notice that the initial discrepancy between the Reynolds stresses in the present simulations and in the DNS of Stanley *et al.* (2002) comes from the fact that we are not prescribing a 'deterministic' forcing in the present case, as discussed above. In agreement with Stanley & Sarkar (2000) we also note that smaller values of initial h/θ_0 (e.g. DNS1) or inlet noise (e.g. DNS0), while causing a delay in the transition, as compared to DNS2, are compensated by higher maximum values of the Reynolds stresses. Despite these differences in the initial conditions, the plateau-value reached in the self-similar regime

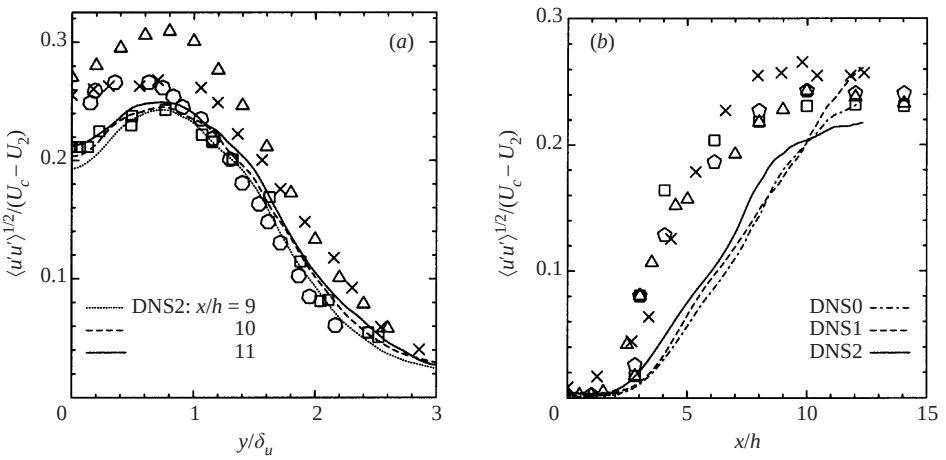

FIGURE 7. (*a*) Streamwise Reynolds stresses profiles for simulation DNS2 at several downstream positions compared with the experimental data from △, Gutmark & Wygnansky (1976), □, Ramprian & Chandrasekhara (1985), ○, Thomas & Chu (1989) and the DNS from ×, Stanley *et al.* (2002) (at $x/h = 10.5$). (*b*) Downstream evolution of the streamwise Reynolds stresses along the centreline for simulations DNS0, DNS1 and DNS2. The simulations are compared with the experimental data from △, Thomas & Chu (1989), ○, Thomas & Prakash (1991) and □, Browne *et al.* (1983), as well as the DNS from ×, Stanley *et al.* (2002).

for DNS0, DNS1 and DNS2 is similar to the values found in previous experimental and numerical studies. The same trend was observed for the lateral and spanwise Reynolds stresses (not shown).

All these validations allow us to consider that our DNS provides an accurate representation of the large-scale dynamics in the self-similar region of spatially developing plane jets.

4.3. *Small scales behaviour*

To assess the accuracy of the present simulations, two banks made up of several instantaneous fields from DNS1 and DNS2 were used to compute the Kolmogorov micro-scale, Taylor micro-scales and the Reynolds number based on the Taylor micro-scale. The Taylor micro-scales vary between $\lambda_x/h \approx 0.1$ and $\lambda_z/h \approx 0.07$. This means that at least 2 to 3 grid points are used to represent the Taylor micro-scale ($\lambda \approx 2$ to $3\Delta x$). This shows that, compared to the mesh size, both the Kolmogorov and Taylor micro-scales are well within the accepted range for an accurate DNS (see e.g. Jiménez *et al.* 1993; Moin & Mahesh 1998). Furthermore, the Reynolds number based on the streamwise Taylor micro-scale is about $Re_{\lambda_x} \approx 100$, for both simulations. Thus, at least from $x/h \geqslant 10$, the simulations DNS1 and DNS2 have a considerable level of small-scale turbulence and can be considered to represent fully developed turbulent (non-transitional) flows.

As an extra test for proper accuracy, we next consider the frequency spectrum of the streamwise velocity component (see figure 8). These time spectra were computed from streamwise velocity signals taken from the simulations DNS1 and DNS2, in the self-similar region ($x/h = 10$). This was made with time series composed of 8000/7500 samples for DNS1/DNS2. For these computations each signal was divided into 5 equally sized time series subsets (1600/1500 samples each). A one-dimensional subspectrum was then calculated for each one of these subsets and the final spectrum was obtained through an ensemble averaging over all the subspectra. This procedure

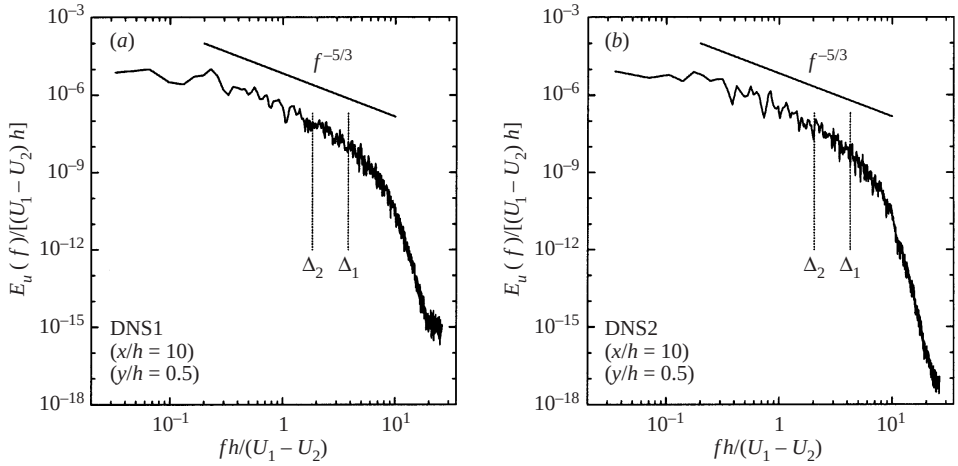

FIGURE 8. Temporal spectra of the streamwise velocity at the far field of the plane jet for simulations DNS1 and DNS2. (*a*) Streamwise velocity spectrum for DNS1 at $x/h = 10$. (*b*) Streamwise velocity spectrum for DNS2 at $x/h = 10$.

was adopted to improve the quality of the statistics for an accurate measure of the spectral slope of the inertial region (if present). The frequency spectra exhibit a well-defined slope close to $-\frac{5}{3}$, which is the signature of an inertial range extending over about one decade. Note that in DNS1, the slope seems to be slightly smaller than $-\frac{5}{3}$ at $x/h = 10$ (see figure 8*a*). This may be explained by the slightly later transition to turbulence observed in DNS1 compared to DNS2. The inertial ranges are followed by a smooth decrease of the energy at high frequencies, which indicates a well-resolved dissipative range. The high-frequency regions do not show any sign of energy accumulation except for the very end of the spectrum where the signal is of comparable intensity to the numerical noise. As pointed out by Moin & Mahesh (1998) 'the requirement to obtain reliable first and second order statistics is that the resolution be fine enough to accurately capture most of the dissipation'; figure 8 leads us to consider that this requirement is indeed met in the present simulations.

As far as frequencies are concerned, we have also checked that the characteristic frequencies of the plane jet are recovered. Although it is difficult to extract the characteristic frequency of the initial instability of the jet shear-layer owing to the high-amplitude of the inlet noise, we may deduce it from the separation length between consecutive Kelvin–Helmholtz billows. For a plane jet, the expected shear-layer instability is associated with a Strouhal number (Monkewitz & Huerre 1982),

$$S_{sl} = \frac{f_{sl}\theta}{U_c} = 0.033, \tag{4.4}$$

where $U_c = 0.5(U_1 + U_2)$ is the convection velocity, and f_{sl} is the frequency associated with the shear-layer mode. In the present cases, with h/θ_0 equal to 30 (DNS0 and DNS2) and 20 (DNS1) this corresponds to an instability length scale of $\lambda_{sl} = \theta/S_{sl}$ equal to $1.0h$, $1.515h$ and $1.0h$ for DNS0, DNS1 and DNS2, respectively. Figure 1(*a*) shows that the primary Kelvin–Helmholtz vortices from DNS0 are located at $x/h \approx 3.2$ and $x/h \approx 4.2$ (see upper shear layer), so that their initial separation is $\lambda \approx 1.0h$, in good correspondence with the theoretical value for the primary instability of the jet shear-layer. For DNS1, the initial separation of the two primary rollers is $\lambda \approx 1.5h$ as shown in figure 1(*b*) (the primary Kelvin–Helmholtz vortices emerge at $x/h \approx 3.5$ and

$x/h \approx 5.0$ at the upper shear-layer). For DNS2, the faster transition process makes the identification of the primary rollers harder, but we can still see that their average separation decreases when compared with the other simulations. The occurrence of merging between the initial Kelvin–Helmholtz vortices makes the situations even more difficult, but a close look at the upper shear layer for DNS2 (see figure 2) shows also the presence of primary Kelvin–Helmholtz vortices at $x/h \approx 3.0$ and $x/h \approx 4.0$ corresponding to an initial separation equal to $\lambda \approx 1.0h$, which agrees also with the theoretically predicted values.

Experimental works on plane jets by Thomas & Goldschmidt (1986), Thomas & Chu (1989), Thomas & Prakash (1991) pointed out the existence of a preferential mode in the self-similar region of the plane jet corresponding to a Strouhal number of,

$$S_{sim} = \frac{f_{sim}\delta_U}{\Delta U} = 0.11. \tag{4.5}$$

Frequency spectra (not shown), computed from the streamwise velocity time series in the far field of the turbulent plane jet for DNS1, show a well-defined peak close to $f^{sim}\delta_U/\Delta U \approx 0.1$ at $x/h = 11$, in agreement with the experimental observations. Similar observation could be made for DNS2.

5. Local grid/subgrid-scale interactions

5.1. *Statistical tools and sample data set*

In this section, the effect of coherent structures upon grid/subgrid-scale interactions will be analysed in the far field of the turbulent plane jet. This will be achieved through a statistical and topological analysis of terms from (2.7) and (2.8), which, as already stressed, are valid locally and instantaneously. As shown in the last section, both the DNS1 and DNS2 simulations are representative of the far-field self-similar region of the turbulent plane jet, but this state is reached earlier in DNS2 than DNS1 owing to the difference in the initial h/θ. To show that the conclusions from the following analysis are independent of this fact, we will make full use of both simulations. Occasionally, we will be interested in the transitional region also, and in this case the simulation DNS0 will be used instead.

For the self-similar region, all the statistical analysis to follow was carried out on data sets made with instantaneous fields from simulations DNS1 and DNS2. The number of instantaneous fields was equal to 373 and 298 for simulations DNS1 and DNS2, respectively. For each instantaneous field, the data was taken from a sampling region placed in the self-similar region of the plane jet ($x/h \approx 10$). This consisted of 10 lines along the spanwise direction (72/80 points each for DNS1/DNS2) both at the upper and lower shear layers. The 10 lines are placed at coordinates $x/h = 9.5$, $x/h = 10$, $x/h = 10.5$ and $y/h = +0.8 \pm 0.04$ and $y/h = -0.8 \pm 0.04$. The total time interval for the instantaneous fields allows for about 5 and 4 Kelvin–Helmholtz vortices to cross the computational domain, both at the upper and lower shear layers for simulations DNS1 and DNS2, respectively. Therefore, the number of samples for each point of the normal (y) profiles is equal to 268 560/238 400 for DNS1/DNS2.

This statistical data set was used to compute the root mean square (r.m.s.), skewness and flatness of each term T, from (2.7) and (2.8). Using the classical Reynolds decomposition of each term $T = \langle T \rangle + T'$, the r.m.s. was made non-dimensional by the reference velocity U_1, and the length scale h,

$$rms = \frac{\langle T'^2 \rangle}{[U_1^3/h]}, \tag{5.1}$$

Term	II Advection	III Diffusion pressure–velocity	IV Viscous diffusion	V Viscous dissipation	VI Diffusion velocity–SGS stresses	VII GS/SGS transfer
r.m.s. $\times 10^{+2}$	+47.0	+19.9	+0.037	+0.0041	+2.37	+0.296
Skewness	−0.88	−0.28	−0.636	−4.00	−0.06	−4.86
Flatness	+14.7	+14.1	+26.7	+39.5	+27.4	+108.0

TABLE 3. Short description of terms from (2.7) in the far field of the turbulent plane jet for simulation DNS1. The root mean square, skewness and flatness were computed with (5.1), (5.2) and (5.3). The statistics were computed using the instantaneous fields from the DNS1 data bank at $x/h = 10$ and $y/h = 0.8$. DNS2 leads to similar results.

Term	IX Advection	X Turbulent transport	XI Diffusion pressure–velocity	XII Viscous diffusion	XIII Viscous dissipation	XIV Diffusion velocity–SGS stresses	XV GS/SGS transfer
r.m.s. $\times 10^{+2}$	+2.50	+2.20	+0.0017	+0.0031	+0.034	+2.37	+0.296
Skewness	−0.25	−0.27	+1.40	+2.44	−2.82	+0.06	+4.86
Flatness	+26.7	+22.1	+36.5	+32.0	+19.9	+27.4	+108.0

TABLE 4. Short description of terms from (2.8) in the far field of the turbulent plane jet. See caption of table 3 for details.

and the skewness and flatness were made non-dimensional by the variance,

$$S = \frac{\langle T'^3 \rangle}{[\langle T'^2 \rangle^{1/2}]^3}, \tag{5.2}$$

$$F = \frac{\langle T'^4 \rangle}{[\langle T'^2 \rangle^{1/2}]^4}. \tag{5.3}$$

The r.m.s., skewness and flatness for the terms from (2.7) and (2.8) are given in tables 3 and 4, respectively. In addition to this, probability density functions (PDFs), joint PDFs and correlation coefficients were computed with several variables. The correlation coefficient between two variables u and v is given by,

$$C_{(u,v)} = \frac{\langle u'v' \rangle}{[\langle u'^2 \rangle \langle v'^2 \rangle]^{1/2}}. \tag{5.4}$$

All the computed correlations are given in table 5. To give an idea of the quality of the sample data, figure 9(a) shows PDFs of the normal velocity (v), the streamwise vorticity (ω_x), and the pressure (p), from the data set based on DNS1. The velocity exhibits a slight sub-Gaussian behaviour, the vorticity is close to exponential and the pressure is asymmetric, having a negative side with higher probability values than the positive side. Very similar features were previously found in homogeneous isotropic turbulence (Métais & Herring 1989; Vincent & Meneguzzi 1991; Métais & Lesieur 1992). Figure 9(b) displays a joint PDF of pressure (p) and vorticity norm (Ω). As expected (see Lesieur 1997), higher values of vorticity are correlated with negative values of pressure owing to the presence of vortical structures. The correlation coefficient is $C_{(p,\Omega)} = -0.51$. Similar results are recovered with DNS2.

Variables	Correlation coefficient	Variables	Correlation coefficient
(p, Ω)	−0.51	$(\|S\|, VII)$	−0.44
$(\Omega, u_i^< u_i^<)$	+0.15	(VI, X)	+0.94
$(\tau_{ii}, u_i^< u_i^<)$	+0.22	(IX, X)	−0.43
(Ω, τ_{ii})	+0.74	(II, X)	−0.24
(II, III)	+0.61	(Ω, XII)	+0.47
(Ω, V)	−0.58	$(\Omega, XIII)$	−0.65
(VI, VII)	−0.24	$(VII, XIII)$	+0.39
$(\tau_{ii}, XIII)$	−0.81	$(VIII + IX, XIII + XV)$	+0.57
		$(u_i^< u_i^<, VII)$	−0.1

TABLE 5. The correlation coefficients. The computations were made with (5.4).

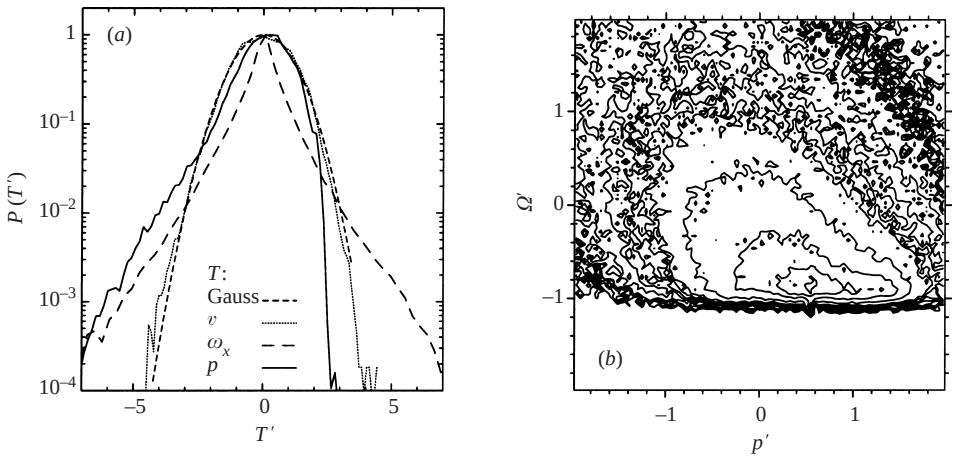

FIGURE 9. Several probability density functions (PDF) and joint PDFs from the DNS1 simulation. The data sample is detailed in the text. For each PDF or joint PDF computation, all variables were removed from their mean values and non-dimensionalized by their respective variances. (*a*) PDFs of the normal velocity (v), the streamwise vorticity (ω_x) and the pressure (p). A Gaussian curve is also shown for comparison. (*b*) Joint PDF of vorticity modulus (Ω) and pressure (p). For all the joint PDFs, 15, logarithmically placed isocontours were used. The isocontours are equally spaced in the range 2×10^{-3} to 1.

Some of the local analysis in the next section, will be carried out also with instantaneous fields exhibiting typical features of the far-field turbulent plane jet. Details of the chosen fields from DNS1 and DNS2 were already shown in figures 3 and 4. Piomelli, Yu & Adrian (1996) used conditional averaging to relate vortical structures from a wall flow with regions of direct/inverse GS/SGS transfer. Unlike wall-bounded flows where some flow events (sweeps, ejections) occur more or less randomly in space and time, the vortical structures of plane jets with which this study is concerned (Kelvin–Helmholtz and streamwise vortices), have relatively long life times. This makes the use of instantaneous fields (instead of conditionally averaged) suitable for this kind of analysis. However, it must be stressed that movies of the analysed quantities were made over sufficiently long time intervals, from which these single instantaneous fields were taken, and lead to the same (qualitative and quantitative) conclusions.

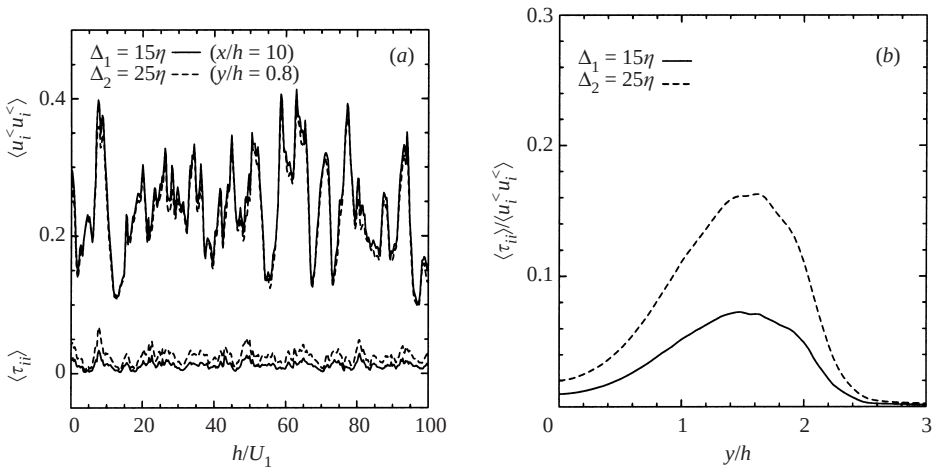

FIGURE 10. (*a*) Temporal evolution of the grid scale and subgrid-scale kinetic energies for the DNS1 simulation at the self-similar region. The kinetic energies were integrated along the spanwise direction. (*b*) Profiles of energy fraction content at the subgrid-scales for the two different filter widths used in this work in the self-similar ($x/h = 10$) region of simulation DNS1.

5.2. *Grid scale and subgrid-scale kinetic energy: topology and statistics*

Before separating GS and SGS, we have to show where the several filters stand concerning energy removal from the GS. This can be analysed first in figure 10(*a*) which serves also to complete the characterization of the DNS1 data bank. The figure displays the temporal evolution of the grid scale and subgrid-scale kinetic energies, integrated along the spanwise direction, using the instantaneous fields used to make the DNS1 data bank. The data were taken from the self-similar region. This figure allows us to observe the statistical steadiness of the DNS1 sample data, both at the large- and small-scales level. The figure shows also that using the two filter widths, the subgrid-scale kinetic energy is much smaller than the grid scale kinetic energy, as is supposed to be the case in a well-resolved LES, which the present work aims at describing. To further clarify this point, figure 10(*b*) displays the ratio of SGS to GS kinetic energy. These profiles were also calculated in the self-similar region of the plane jet for DNS1. DNS2 leads to similar results. The first filter width corresponds to $\Delta_1 = 15\eta$. Using this filter, we have around 7% of the energy at the small scales which is representative of a very fine LES. The second filter width is $\Delta_2 = 25\eta$, and leads to around 16% of the energy at the small-scales level which is representative of a typically good LES (Piomelli *et al.* 1996). At this point, it may be interesting to see where the two filters are placed in the kinetic energy spectrum. A rough idea can be given in figure 8. The figure shows that the two filters are placed in the inertial range region, arguably, the correct place in an LES. Note that the two filter frequencies were computed using Taylor's frozen flow hypothesis, which is not really applicable here because of the very high level of turbulence present at $x/h = 10$. Therefore, interpretation of the real location of the filter frequencies in figure 8 has to be taken with some caution. Finally, it was seen throughout this work that all the topological and statistical results showed only small differences when changing filters (Δ_1 or Δ_2). Moreover, both filter widths are within values commonly used in this type of study (Akhavan *et al.* 2000). Therefore, both filters will be used throughout this work.

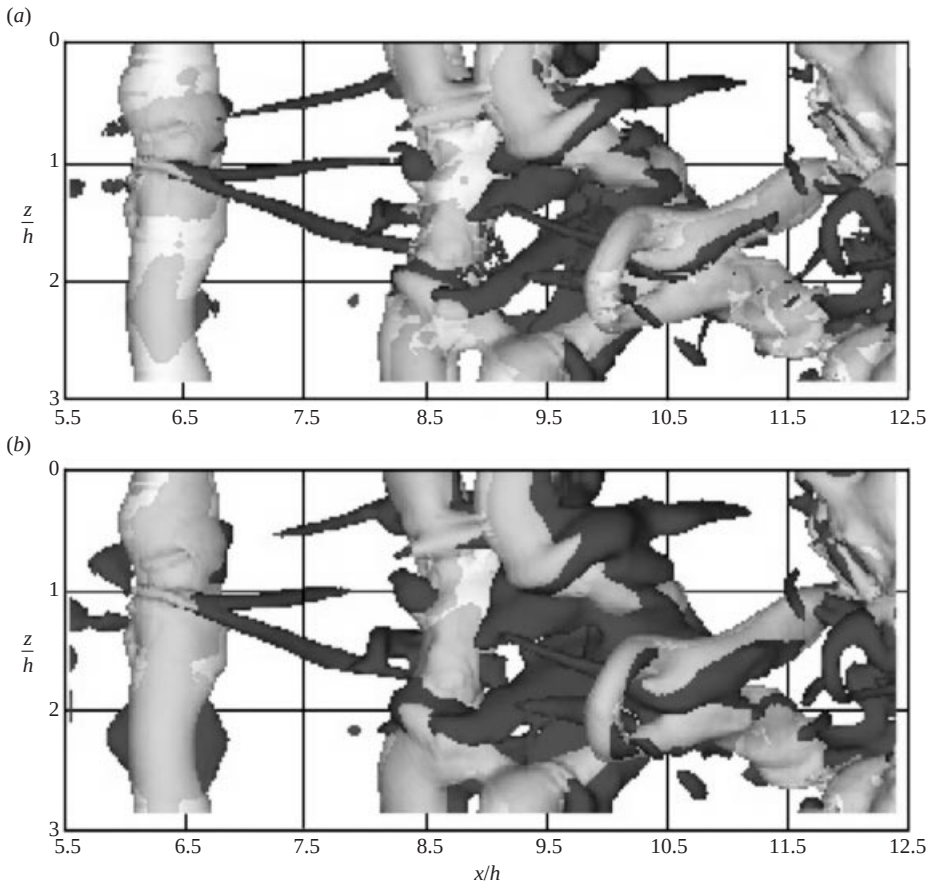

FIGURE 11. Isosurfaces of low pressure p (white grey) in the upper shear layer ($y/h > 0$) and subgrid-scale kinetic energy τ_{ii} (dark grey) for the two filter widths in simulation DNS1. Top view. (a) Filter width $\Delta_1 = 15\eta$. The threshold for τ_{ii} is $+0.2U_1^2$ and τ_{ii} varies between $\tau_{iimin} = 0.U_1^2$ and $\tau_{iimax} = 0.241U_1^2$. ($b$) Filter width $\Delta_2 = 25\eta$. The threshold for τ_{ii} is $+0.3U_1^2$ and τ_{ii} varies between $\tau_{iimin} = 0.U_1^2$ and $\tau_{iimax} = 0.279U_1^2$. Both figures report the same instant which also corresponds to the instant of figure 3. The threshold for the pressure is the same as in figure 3. Note that the pressure was made transparent (70% opacity) to help visualizations.

Figure 11 shows isosurfaces of SGS kinetic energy for the two previously defined filters. We can see clearly that the higher values of the SGS kinetic energy are concentrated in the centre of the coherent structures. This is apparent from the joint PDF of vorticity modulus (Ω) and SGS kinetic energy (τ_{ii}) shown in figure 12 and by their strong correlation coefficient, $C_{(\Omega,\tau_{ii})} = +0.74$. Similar spatial structure was observed recently for the component τ_{12} of the SGS tensor, in a mixing layer by Guerts, de Bruin & Sarkar (2000). At first glance, this seems surprising since there is no clear correlation between the total GS kinetic energy and the coherent structures of the flow. Observation of the isosurfaces of total (mean and fluctuating) GS kinetic energy (not shown) shows that the GS kinetic energy peaks are placed in the centre of the jet ($y/h \approx 0$), with no apparent connection with the presence of the vortices. This lack of correlation is confirmed by the slim correlation coefficient between GS kinetic energy and the vorticity norm ($C_{(\Omega,u_i^< u_i^<)} = +0.15$). When looking into the averaged values of GS and SGS kinetic energy, the same observation can be made

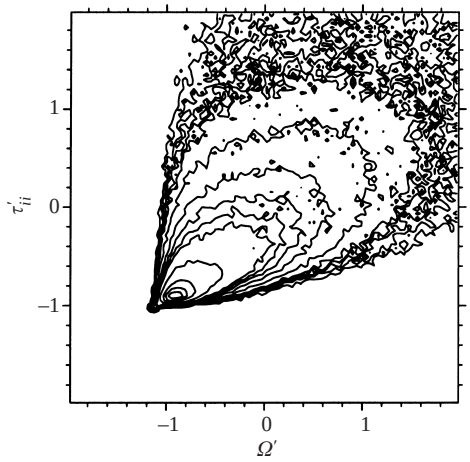

FIGURE 12. Joint PDF of vorticity modulus (Ω) and subgrid-scales kinetic energy (τ_{ii}) for DNS1. The scales were separated with filter width $\Delta_2 = 25\eta$. In calculating the PDF, both variables were removed from their mean values and non-dimensionalized by their respective variances. For this joint PDF, 15, logarithmically placed isocontours were used. The isocontours are equally spaced in the range 2×10^{-3} to 1.

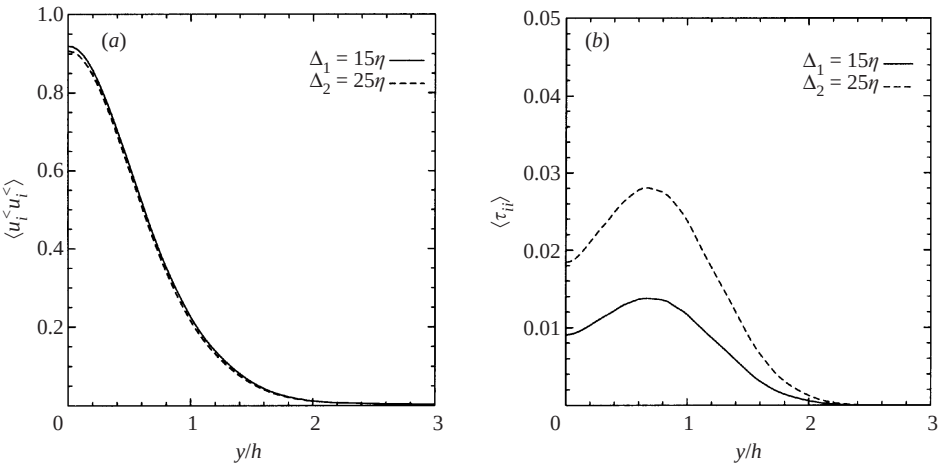

FIGURE 13. (*a*) Profiles of grid scale kinetic energy for the two filter widths in DNS1 at $x/h = 10$. (*b*) Profiles of subgrid-scale kinetic energy for the two filter widths in DNS1 at $x/h = 10$.

(see figure 13). Compared to the large scales, there is a very small amount of energy in the small scales, and wider filters lead to more energy in the SGS and less in the GS, as expected. However, the shape of the two curves is quite different. Most of the GS kinetic energy is to be found at the centre of the shear layer whereas in the SGS its maximum is located in the region of the shear-layer gradients. Thus, it is clear that in a statistical sense, GS and SGS kinetic energy are also uncorrelated. The same happens at a local level, as can be seen by the weak correlation coefficient between these two quantities, $C_{(\tau_{ii}, u_i^< u_i^<)} = +0.22$.

Now, if the SGSs are highly correlated with the large coherent structures, which are clearly large-scale (GS) events, this means that the small-scale dynamics are being highly affected by large-scale processes. In what follows, some observations are put forward in order to shed new light upon this GS/SGS dynamics.

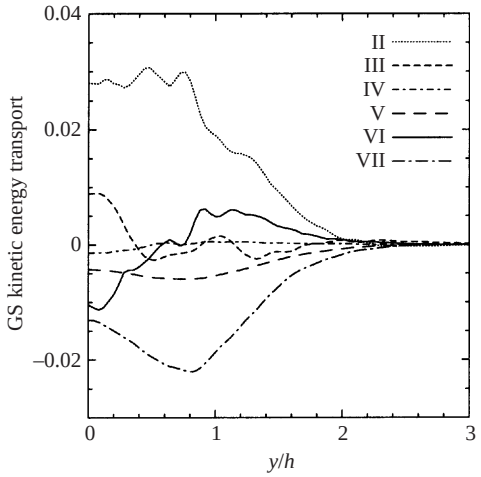

FIGURE 14. Profiles of averaged terms from (2.7) for DNS2, at $x/h = 10$, in the far field of the plane jet. The filter width is $\Delta_2 = 25\eta$ and the averaging was carried out along the homogeneous direction and the symmetry plane (x, z) and over 298 instantaneous fields from DNS2.

5.3. *Coherent structures and large-scale dynamics*

A first picture of the GS dynamics can be gained by looking at the profiles of the averaged terms from (2.7) in the far field of the turbulent plane jet ($x/h = 10$). These are shown in figure 14 for simulation DNS2. Here, the averaging consists of a spatial averaging along the spanwise direction (80 points) and a temporal averaging using several (298) instantaneous fields so that the resulting profiles are functions of y/h. In addition to this, averaging is also made along the plane jet symmetry plane (x, z). A complete convergence of such profiles requires a very long time integration (Piomelli *et al.* 1996). Although our statistics are not completely converged, the degree of convergence is sufficient to show the global trends. Since the flow is statistically stationary, term I averaged in this way is zero everywhere and therefore is not shown in the figure.

Figure 14 shows that, in the mean, the terms II (GS kinetic energy advection), III (GS pressure/velocity interactions), VI (GS/SGS diffusion) and VII (GS/SGS transfer) are clearly dominant. Conversely, the terms V (GS viscous dissipation) and IV (GS viscous diffusion) are, on average, negligible. This is what we may expect to obtain in a well-resolved LES where the effects of molecular viscosity are negligible as far as the GS dynamics are concerned. Another expected result is that the term VII (GS/SGS transfer) is found to be quite significant and always negative. With the sign convention used here, negative values for the term VII (and VI) correspond to a kinetic energy transfer from GS to SGS (forward scatter), whereas positive values are associated with a transfer from SGS to GS level (backward scatter). Therefore, in the mean, the GS/SGS transfer (term VII) corresponds solely to forward scatter. The first surprise comes from the other term directly related with GS/SGS kinetic energetic exchanges. Indeed, the averaged term VI (GS/SGS diffusion) displays extrema of the same order of magnitude as term VII. In virtually all the studies devoted to SGS modelling, term VI is assumed to be less important than term VII (Piomelli *et al.* 1996; Akhavan *et al.* 2000; Meneveau & Katz 2000). It is argued that this term, being a redistribution term (that integrates to zero in the whole domain), has only a negligible effect in the GS/SGS interactions. This was shown to be the case in

near-wall flows (Balaras & Piomelli 1994), but to our knowledge, this has never been checked before in free shear flows. Figure 14 also displays large variations of term VI with y/h. Indeed, near the jet centreline, $|y/h| < +0.6$, on average, term VI contributes to forward scatter, whereas in the interval $0.6 < |y/h| < 1.8$ it contributes to a strong mean backscatter. One possible explanation could be that, in free shear flows, the transport terms, which are not inhibited by the presence of a wall, generally play a more important role than in wall-bounded flows.

We now turn into the analysis of the local behaviour of the various terms from (2.7). A measure of the local fluctuating intensity of the terms is provided by their r.m.s. values. These are given in table 3. It can be seen immediately that the local intensities of terms II and III ($rms_{II} = +47.0 \times 10^{-2}$ and $rms_{III} = +19.9 \times 10^{-2}$) are much larger than all the other terms. At a second level of importance come terms VI ($rms_{VI} = +2.37 \times 10^{-2}$) and VII ($rms_{VII} = +0.296 \times 10^{-2}$). The fact that $rms_{VI} \gg rms_{VII}$ shows unambiguously that GS/SGS diffusion (VI) has a greater local importance than the GS/SGS transfer (VII). This is a somewhat surprising result which could not be deduced only by examining the averaged profiles. This implies that local and instantaneous flow events such as coherent structures, for instance, are likely to have a stronger impact on the GS evolution through GS/SGS diffusion (VI) rather than through GS/SGS transfer (VII). This has consequences for SGS modelling analysis; the performance of a given SGS model to describe correctly the local flow events (e.g. the flow structures) should be evaluated by comparing the modelled and the real terms VI, and not only the modelled and the real terms VII as is usually done in *a priori* tests. Finally, concerning now the terms related to molecular viscosity (IV and V), we notice that they both have very small r.m.s. values ($rms_{IV} = +0.037 \times 10^{-2}$ and $rms_V = +0.0041 \times 10^{-2}$). Thus, in the mean as well as locally, the terms IV and V play a negligible role in the GS dynamics.

Table 3 also provides information regarding the local behaviour of all the terms of (2.7). The skewness factor S, being a measure of the asymmetry of the probability density function, shows that most of the terms exhibit similar levels of asymmetry (e.g. terms II, III and IV with $S_{II} = -0.88$, $S_{III} = -0.28$, $S_{IV} = -0.636$). It is interesting to note that these values are close to the skewness of the filtered velocity gradients found in a high-Reynolds-number wake flow (Cerutti, Meneveau & Knio 2000). However, two terms in particular exhibit much higher skewnesses. These are terms V ($S_V = -4.0$) and VII ($S_{VII} = -4.86$). This asymmetry is attributable to the fact that the term V is always a sink of GS kinetic energy and that forward scatter dominates over backward scatter for the term VII. The flatness factor F allows us to measure the departure from Gaussianity and then constitutes an indication of the intermittent nature of the measured quantity (for a Gaussian distribution $F = 3$). The values of F are very high values for the terms related to molecular viscosity ($F_{IV} = +26.7$ and $F_V = +39.5$) and also for the term VII ($F_{VII} = +108.0$). High intermittency for terms IV and V occurs because viscosity must 'kill' the relatively rare events associated with very high GS velocity gradients. The intermittent nature of term VII can be more precisely analysed through figure 15. The figure shows the probability density function of terms VI and VII. We can see that the PDF of term VI is only slightly asymmetric ($S_{VI} = -0.06$) and has a moderate intermittent level ($F_{VI} = +27.4$) compared to the other terms of the equation. It was checked that most terms have PDFs of shape very similar to term VI (not shown). It is worth noting the particular shape of the PDF of term VII with a very different behaviour for the negative tail associated with the forward scatter ($T'_{VII} < 0$) and for the positive tail representing backscatter ($T'_{VII} > 0$). The rapid drop of the backscatter tail for

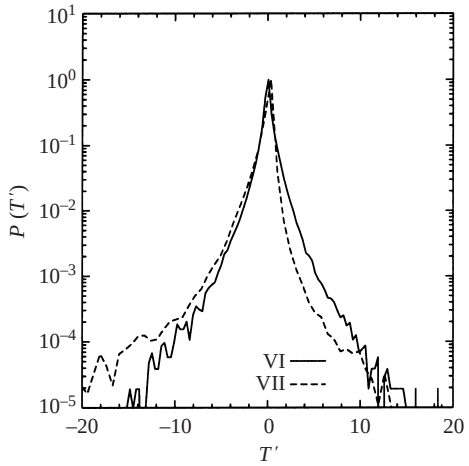

FIGURE 15. Probability density functions (PDF) of terms VI and VII from (2.7). Each PDF was divided by its maximum value to allow comparison between the several curves. Both terms T, were removed from their mean values and non-dimensionalized by their variances. The filter width was $\Delta_2 = 25\eta$. The PDFs were computed using the instantaneous fields from the DNS1 data bank at $x/h = 10$ and $y/h = 0.8$. DNS2 leads to similar results.

small and intermediate values of VII and the nearly exponential wings for the largest values indicate not only that forward scatter is a more frequent event than backward scatter (as expected), but that backscatter acts as very rare but strong fluctuations, with the nearly-zero backscatter events being the most likely. Indeed, by comparing the PDF curves for terms VI and VII, we can say the high value of the intermittency of term VII comes mainly from its backscatter tail.

We now examine how the various terms of (2.7) relate to the presence of coherent structures. Let us start with term III accounting for GS pressure–velocity interactions and which corresponds, as shown above, to one of the most significant terms (behind II) as far as local values are concerned. An instantaneous picture of the values from this term is shown in figure 16. The picture shows isosurfaces of low pressure (the same as in figures 3 and 4) and isosurfaces of negative/positive term III (blue/red). As before, with the sign convention used here, negative/positive values represent loss/gain of GS kinetic energy. The first observation, which proves to be common to the most important terms, is that their higher values are not randomly distributed in space. For term III, the stronger intensities appear in the vicinity of the flow coherent vortices. The positive and negative peaks are not located at the centre of the vortices but ahead and behind (or on top and bottom) of them. Moreover, the peaks of strong positive values appear close to the strong negative ones, the interface of these regions being the very centre of a vortical structure. Although this can be seen to be happening both for the large Kelvin–Helmholtz rollers and for the smaller, more intense, streamwise vortices, it seems this term is more sensitive to the presence of the large rollers than to the smaller vortices, as most of its high values are found primarily near these large structures. It was noticed (not shown) that term II (GS kinetic energy advection) displays a similar behaviour. This can be seen with the joint PDF of both terms shown in figure 17(a). The correlation coefficient (see table 5) is $C_{(II,III)} = -0.61$. As previously emphasized, the terms II and III were found to be among the most important as far as mean (averaged) and local (r.m.s.) values are concerned. Their spatial correlation with the large coherent structures can be easily

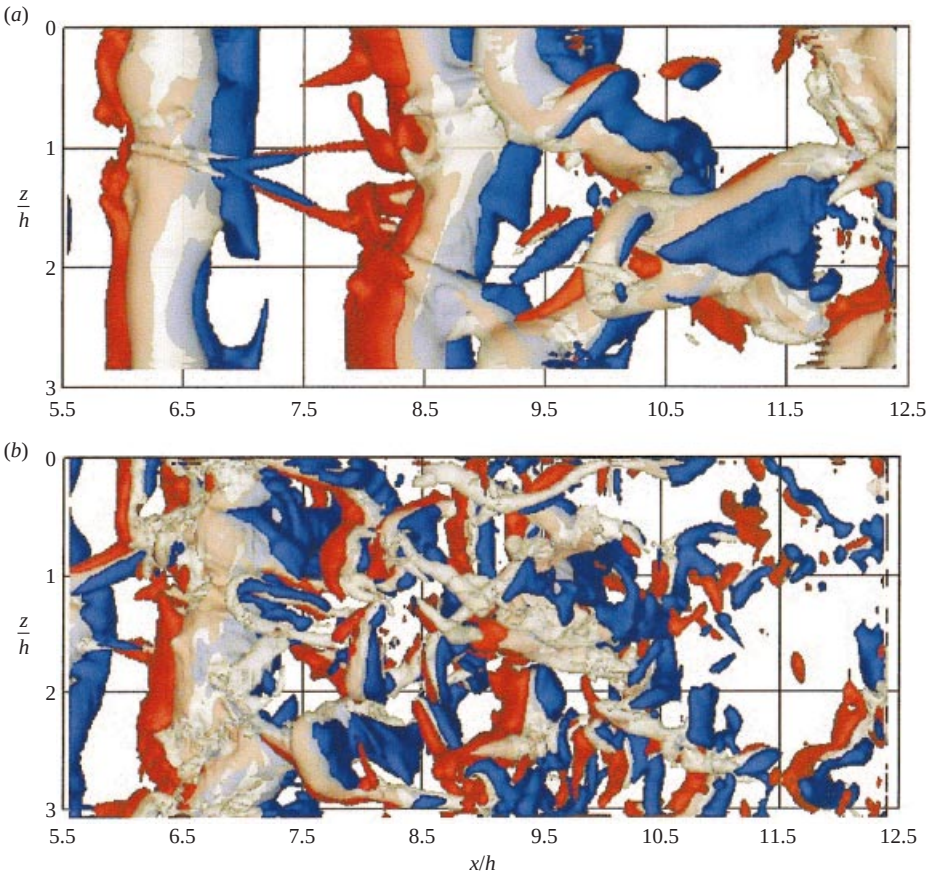

FIGURE 16. Visualizations of term III – GS diffusion by pressure–velocity interactions (blue/red) and low pressure (grey) in the upper shear layer (top view) for DNS1 and DNS2. The figures correspond to the same instant as in figures 3(*a*) and 4(*a*), respectively, but the pressure isosurfaces were made transparent (75% opacity) to help visualizations. The filter width is $\Delta_1 = 15\eta$. (*a*) Term III in DNS1. The threshold for term III is the following: blue corresponds to $-0.8U_1^3/h$, red corresponds to $+0.8U_1^3/h$ and term III varies between $T_{min} = -64.2U_1^3/h$ and $T_{max} = +22.6U_1^3/h$. (*b*) Term III in DNS2. The threshold for term III is the following: blue corresponds to $-0.8U_1^3/h$, red corresponds to $+0.8U_1^3/h$ and term III varies between $T_{min} = -33.5U_1^3/h$ and $T_{max} = +22.8U_1^3/h$.

understood. Indeed, it is commonly agreed that the large coherent structures are responsible for most of the transport of total (large- and small-scale) kinetic energy and this topological analysis showed that terms II and III have most of their activity near these larger flow vortices (here, the Kelvin–Helmholtz vortices). It is reasonable to suppose that the GS advection will be enhanced by the local velocity increase produced by the presence of these large structures. The fact that GS pressure–velocity interactions increases near the large rollers may be caused by the conjunction of the high level of small-scale turbulence inside the rollers (see figures 3 and 4) and with the high-pressure gradient located in their neighbourhood.

We now turn to the spatial localization of terms VI (GS/SGS diffusion) and VII (GS/SGS transfer), which were shown to be after terms II and III in terms of local magnitudes. As already stressed, these terms represent the kinetic energy exchanges between GS and SGS. Figure 18 shows isosurfaces of term VII (red/blue) and positive Q (same as in figures 3*b* and 4*b*). As before, positive/negative isosurfaces of the term

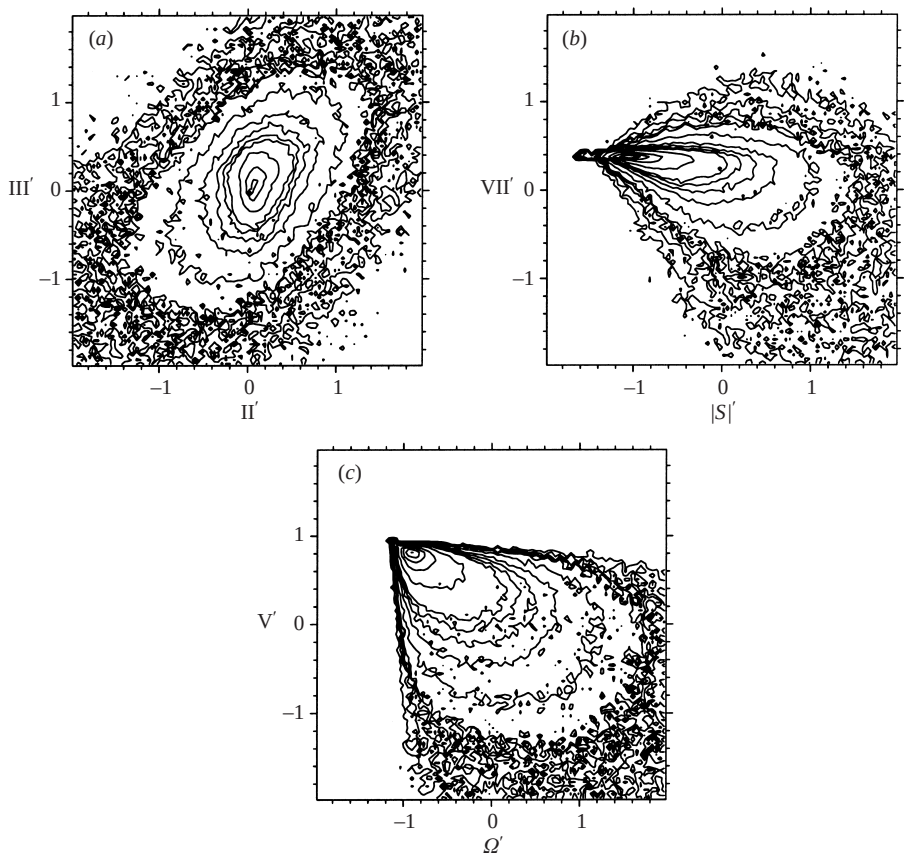

FIGURE 17. Several joint probability density functions (PDF) of terms from (2.7). For each joint PDF computation, all variables were removed from their mean values and non-dimensionalized by their respective variances. The PDFs were computed using the instantaneous fields from the DNS1 data bank at $x/h = 10$ and $y/h = 0.8$. DNS2 leads to similar results. For all the joint PDFs, 15, logarithmically placed isocontours were used. The isocontours are equally spaced and range from 2×10^{-3} to 1. The filter width was $\Delta_2 = 25\eta$. (*a*) Joint PDF of terms II and III. (*b*) Joint PDF of strain rate ($|S|$) and term VII. (*c*) Joint PDF of vorticity modulus (Ω) and term V.

are shown in red/blue, which, for this term (as well as for VI), represent backward and forward scatter, respectively.

The first surprising observation is that VII (GS/SGS transfer) shows no clear sign of correlation with the coherent structures. This seems to contradict some of the previous numerical and experimental observations. O'Neil & Meneveau (1997) observed a strong correlation between the big billows in a Kármán-street of a turbulent wake and the so-called 'surrogate' subgrid-scale dissipation ($\tau_{11}S_{11}^{<}$). Horiuti (1996, 1997) also noted a strong correlation between the coherent structures and what he defined as the 'SGS production' ($P_{ij} = (u_i^{<}u_j^{<})^{<}\ \partial u_i^{<}/\partial x_j$). A possible explanation for this unexpected result found in our simulation comes from the fact that in the present case the structures are 'more random' and not so 'nicely periodic' as in O'Neil & Meneveau (1997) and Horiuti (1997). Indeed, the present simulation corresponds to a fully developed turbulent flow configuration whereas some transitional structures may still be present in the works of O'Neil & Meneveau (1997) and Horiuti (1997). Let us note also that O'Neil & Meneveau (1997) stressed that the good correlation between

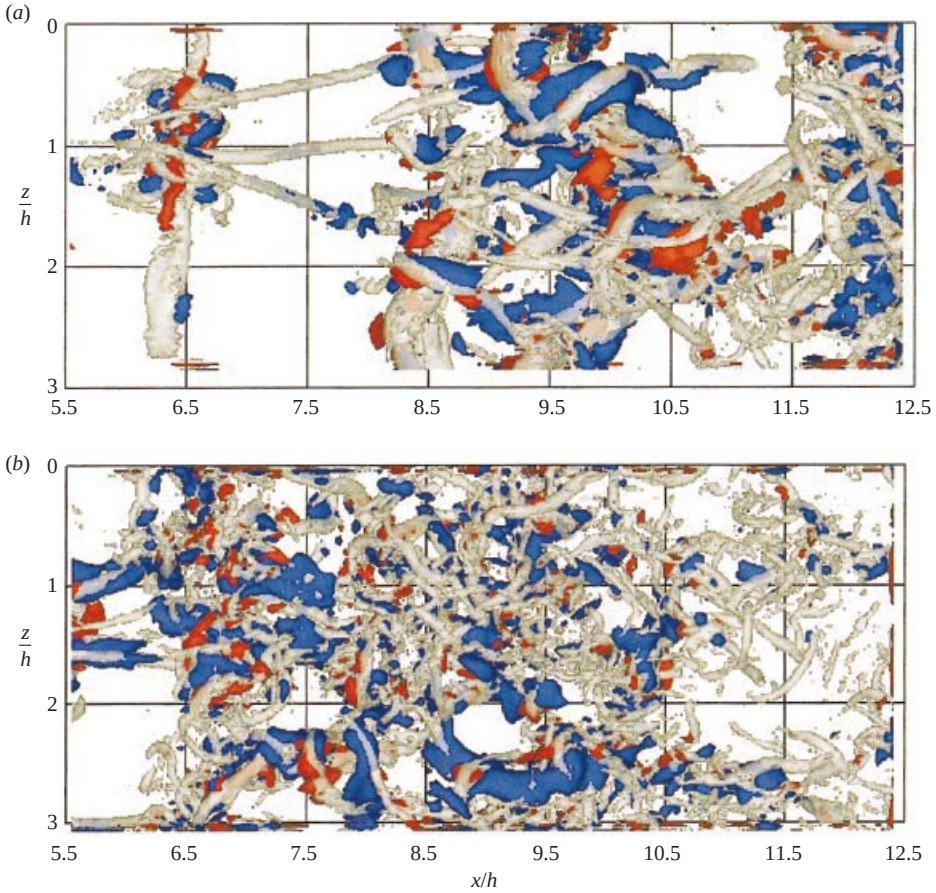

FIGURE 18. Visualizations of term VII – GS/SGS transfer or 'SGS dissipation' (blue/red) and positive Q criterion (grey) in the upper shear layer (top view) for DNS1 and DNS2. The figures correspond to the same instant as in figures 3(b) and 4(b), respectively, but the Q isosurfaces were made transparent (75% opacity) to help visualizations. The filter width is $\Delta_1 = 15\eta$. (a) Term VII in DNS1. The threshold for term VII is the following: blue corresponds to $-0.05U_1^3/h$, red corresponds to $+0.015U_1^3/h$ and term VII varies between $T_{min} = -2.24U_1^3/h$ and $T_{max} = +0.49U_1^3/h$. (b) Term VII in DNS2. The threshold for term VII is the following: blue corresponds to $-0.1U_1^3/h$, red corresponds to $+0.025U_1^3/h$ and term VII varies between $T_{min} = -1.86U_1^3/h$ and $T_{max} = +2.11U_1^3/h$.

$\tau_{11}S_{11}^{<}$ and the Kármán billows was seen in a flow region where the structures were still clearly defined, but they pointed out that further downstream, when coherent structures cease to be nicely organized, this might not be the case. Horiuti (1996, 1997) explained the good correlation he found between the 'SGS production' and the streamwise vortices by the particular shape of the 'well defined' field of background deformation rate S_{ij}, created by the presence of the streamwise structures. In the present simulation, the coherent structures are embedded in a much more complex field of background deformation rate. This can be seen for instance in the joint PDF of term VII and the deformation rate,

$$|S| = \left(2S_{ij}S_{ij}\right)^{1/2}, \tag{5.5}$$

shown in figure 17(b). Although, there is some degree of (anti) correlation between these two quantities, the correlation coefficient is not very high, $C_{(VII,|S|)} = -0.44$.

Note that even in the present simulation, in the transition region where the background deformation rate is not yet very complex, a good correlation between term VII and the streamwise structures could also be seen, as in O'Neil & Meneveau (1997) and Horiuti (1996, 1997). To this end, figure 19 shows term VII in the transition region for DNS0. The figures show that strong forward scatter (term VII < 0) occurs preferentially in regions of high local velocity gradients created by the presence of the streamwise vortices, in agreement with Horiuti (1997).

From this discussion, it seems that although there is a natural tendency for the term GS/SGS transfer to be correlated with the vortical structures, because its definition involves the GS rate of deformation tensor $S_{ij}^{<}$ which has a well-defined shape near a vortex, as the flow evolves into fully developed turbulence, this correlation will tend to decrease owing to the increasing level of complexity of the background turbulence.

Returning to figure 18, we can see with the positive/negative isosurfaces level, that there are more numerous regions, and of more intense magnitude, of forward than backward scatter, in agreement with the PDF of term VII shown above. We note also that as in Piomelli *et al.* (1996), the two types of transfer occur in close proximity to each other and strong backward scatter regions are generally surrounded by regions of high forward scatter. Note that the three-dimensional distribution of term VII for simulation DNS0 in the self-similar region gave similar results, which demonstrates that the above results are independent of the inlet noise amplitude.

As previously discussed, the term VI (GS/SGS diffusion) was shown to have higher local intensities (r.m.s.) than term VII; it is then expected to play a major role in the local GS dynamics. Figure 20 shows isosurfaces of negative/positive (blue/red) values of VI which correspond to local forward/backward scatter (positive Q criterion is also shown as in figures 3*b* and 4*b*). The figure shows that unlike term VII, term VI is clearly correlated with the presence of the vortical structures. Intense regions of term VI are located next to the vortex cores (not in their centres). Term VI seems to be more sensitive to the presence of the streamwise structures than to the large Kelvin–Helmholtz billows, contrary with what happens with terms II and III. As shown by the PDF of term VI shown in figure 15, the isosurfaces confirm that backscatter is of comparable magnitude to forward scatter. It is important to notice the low level of correlation between terms VI and VII: the correlation coefficient is only $C_{(VI,VII)} = -0.24$ (see table 5). This low value shows that GS/SGS transfer and GS/SGS diffusion are not only quite different physical processes, but also take place at very different flow locations and thus seem to be participating into very different physical processes. For example, as seen here, the passage of a coherent structure does not seem to influence the behaviour of GS/SGS transfer (term VII), but has a great influence in the GS/SGS diffusion (term VI). Now, the passage of a vortical structure is an example of a local flow event. Because (i) term VI has greater local intensities (r.m.s.) than term VII and (ii) term VI has its higher values right next to the flow vortices (whereas term VII is not correlated with these) it is fair to say that the evolution of these vortical structures is more affected through term VI than term VII.

To end this section on GS dynamics some comments are also made about the spatial localization of the remaining terms (IV, V) of (2.7), which, as shown above, are negligible both from a global (mean) and local (instantaneous) point of view. The GS viscous diffusion (term IV) was not found to be correlated with the vortical structures (not shown). On the other hand, the GS viscous dissipation (term V) exhibits some correlation with the vortical structures (figure 21). This term always has negative values as expected, since it represents a sink of GS kinetic energy. It seems this GS

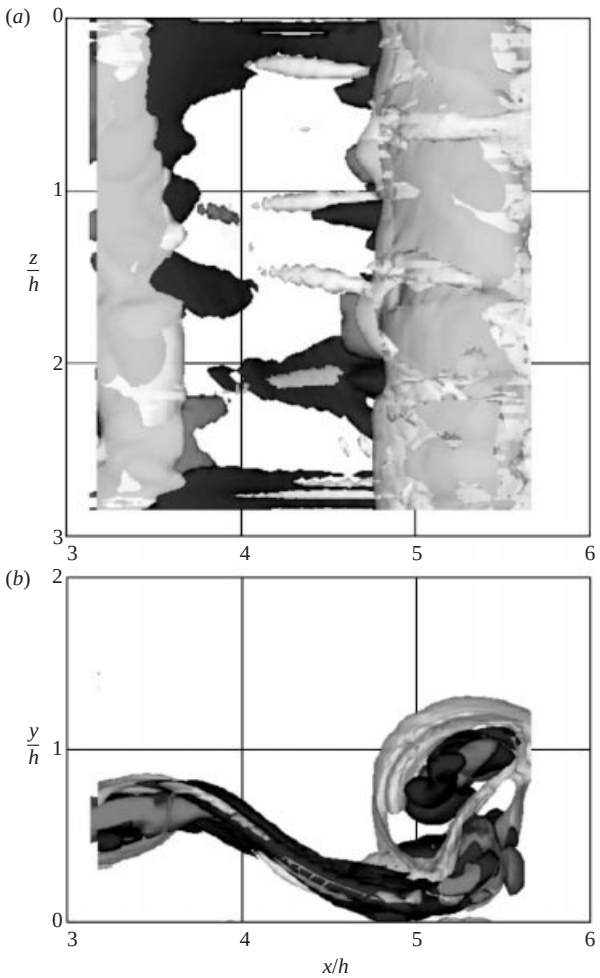

FIGURE 19. Visualizations of term VII – GS/SGS transfer or 'SGS dissipation' (dark/grey) and positive Q criterion (white) in the upper shear layer ($y/h > 0$) in the transition region for DNS0. The figure shows only the region $3 < x/h < 6$ (and $0 < z/h < 3$). The positive Q isosurface was made transparent (75% opacity) to help visualizations. The filter width is $\Delta_1 = 15\eta$. The threshold for Q is equal to $+0.00015(U_1/h)^2$ and Q varies between $Q_{min} = -311(U_1/h)^2$ and $Q_{max} = +889(U_1/h)^2$. The threshold for term VII is the following: dark corresponds to $-0.005U_1^3/h$, grey corresponds to $+0.005U_1^3/h$ and term VII varies between $T_{min} = -5.1U_1^3/h$ and $T_{max} = +2.5U_1^3/h$. (*a*) Top view. (*b*) Side view.

viscous dissipation occurs mainly inside the vortex cores. This can be explained by writing the Reynolds averaged Navier–Stokes equations in cylindrical coordinates, for an isolated vortex in a Galilean reference frame having its origin at the centre of the vortex core. In the absence of axial velocity gradients, the production term of kinetic energy is given by (Zeman 1995),

$$P_{r\theta} = -\langle v'_\theta v'_r \rangle \left(\frac{\partial \langle v_\theta \rangle}{\partial r} - \frac{\langle v_\theta \rangle}{r} \right). \tag{5.6}$$

Here, the angle brackets represent averaging made along the tangential direction. θ and r represent the tangential and radial directions, respectively. Since the tangential

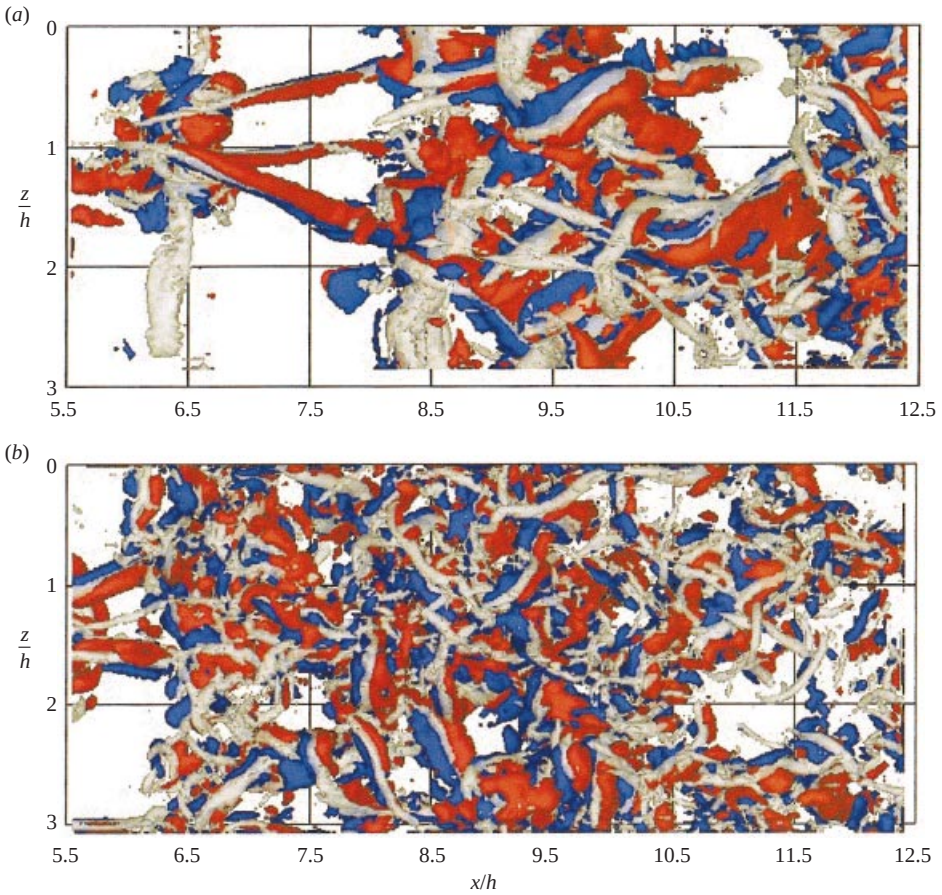

FIGURE 20. Visualizations of term VI – GS velocity–SGS stresses interactions (blue/red) and positive Q criterion (grey) in the upper shear layer (top view) for DNS1 and DNS2. The figures correspond to the same instant as in figures 3(b) and 4(b), respectively, but the Q isosurfaces were made transparent (75% opacity) to help visualizations. The filter width is $\Delta_1 = 15\eta$. (a) Term VI in DNS1. The threshold for term VI is the following: blue corresponds to $-0.1U_1^3/h$, red corresponds to $+0.1U_1^3/h$ and term VI varies between $T_{min} = -4.1U_1^3/h$ and $T_{max} = +3.0U_1^3/h$. (b) Term VI in DNS2. The threshold for term VI is the following: blue corresponds to $-0.15U_1^3/h$, red corresponds to $+0.15U_1^3/h$ and term VI varies between $T_{min} = -6.9U_1^3/h$ and $T_{max} = +2.5U_1^3/h$.

velocity grows linearly with r, within the vortex core region,

$$\langle v_\theta \rangle \propto r, \tag{5.7}$$

it follows that there is no turbulent production. Moreover, the local Reynolds number in the vortex core region is always quite low, owing to the zero tangential velocity at the centre of the vortex. This implies that all turbulence existing in the core region of a circular vortex with no axial velocity gradients must come from the surrounding turbulent field that is wrapped into it. Therefore, the core of the vortices is a region of potential strong viscous dissipation. This agrees with what has been seen numerically and experimentally for the total (large and small scales) kinetic energy viscous dissipation (Kawahara *et al.* 2000). The degree of correlation between term V and the vorticity norm can be seen in their joint PDF shown in figure 17(c). The correlation coefficient between the vorticity modulus and term V is quite high,

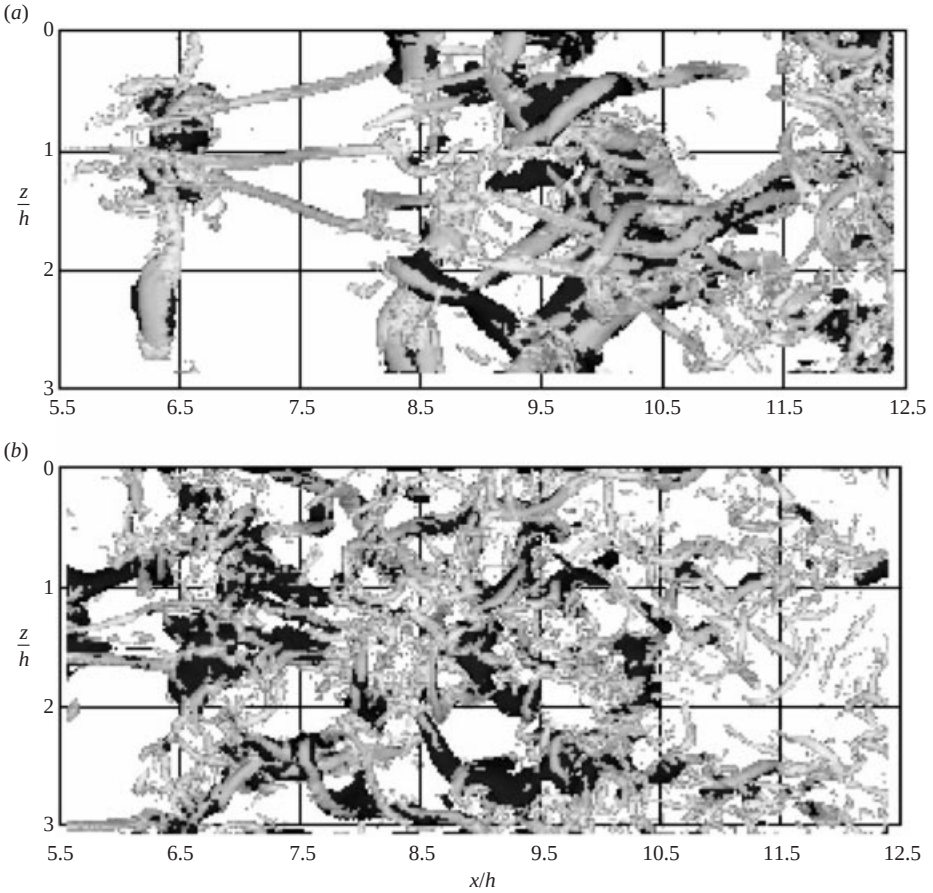

FIGURE 21. Visualizations of term V – GS viscous dissipation (dark) and positive Q criterion (grey) in the upper shear layer (top view) for DNS1 and DNS2. The figures correspond to the same instant as in figures 3(b) and 4(b), respectively, but the Q isosurfaces were made transparent (75% opacity) to help visualizations. The filter width is $\Delta_1 = 15\eta$. (a) Term V in DNS1. The threshold for term V is the following: dark corresponds to $-0.025U_1^3/h$ and term V varies between $T_{min} = -4.48U_1^3/h$ and $T_{max} = 0$. (b) Term V in DNS2. The threshold for term V is the following: dark corresponds to $-0.035U_1^3/h$ and term V varies between $T_{min} = -4.6U_1^3/h$ and $T_{max} = 0$.

$C_{(\Omega,V)} = -0.58$. Note, however, that the GS viscous dissipation is taking place in other regions. Moffatt, Kida & Ohkitani (1994) showed that part of the total kinetic energy viscous dissipation occurs also in the region of high velocity gradients, nearby the vortical structures. A closer look into our results shows the same trend. Therefore, the GS viscous dissipation (term V) occurs mainly at the centre but also in the region just outside the vortex cores.

5.4. *Coherent structures and small-scale dynamics*

The various terms of (2.8) will be now analysed. The averaged profiles of all the terms (except term VIII whose averaged profile is zero) computed in the far field of the turbulent jet are shown in figure 22. The averaging procedure is identical to that applied to obtain figure 14. As expected in an energy cascade process, we verify the mean (global) equilibrium assumption, which states that all the kinetic energy arriving at the SGS due to the GS/SGS transfer (term XV – symmetric of term VII) has to

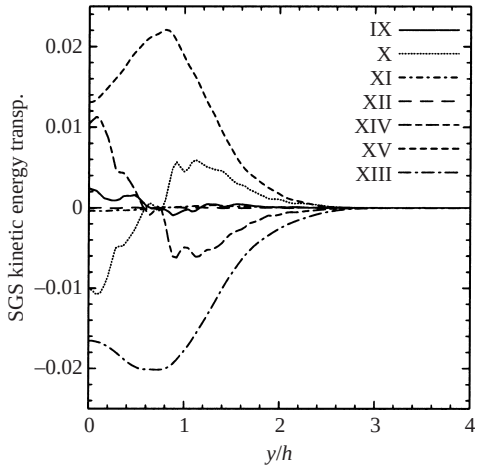

FIGURE 22. Profiles of averaged terms from (2.8) for DNS2, at $x/h = 10$, in the far field of the plane jet. The filter width is $\Delta_2 = 25\eta$ and the averaging was carried out along the homogeneous direction and the symmetry plane (x, z) and over 298 instantaneous fields from DNS2.

be dissipated by the viscous SGS dissipation (term XIII). The second observation concerns the terms XIV (GS/SGS diffusion – symmetric of term VI) and X (SGS turbulent diffusion). These two terms are in almost perfect statistical (and local – as will be seen later) equilibrium. This equilibrium was already observed by Balaras & Piomelli (1994) in a wall flow. It is worth noticing that it also holds in a free shear layer, for which unlike the wall-layer region in a wall flow, there is no statistical equilibrium between production and dissipation of (total) kinetic energy (Tennekes & Lumley 1972). The last group of importance is constituted by the terms IX (SGS advection), XI (SGS pressure–velocity interactions) and XII (SGS viscous diffusion). Term IX seems to be transferring SGS kinetic energy from $|y/h| \approx 0.8$ into the centre of the shear layer ($|y/h| \approx 0$). Even if in the mean, term IX has some importance in the interval $|y/h| < 0.8$, this last group of terms can be considered to be negligible for the dynamics of the mean SGS.

We now turn to the r.m.s., skewness and flatness of the various terms (summarized in table 4). As far as fluctuations are concerned, the most intense terms are IX ($rms_{IX} = 2.50 \times 10^{-2}$), X ($rms_X = 2.20 \times 10^{-2}$) and XIV ($rms_{XIV} = 2.37 \times 10^{-2}$). The high local magnitude (r.m.s.) of the term IX (SGS advection) is surprising since this term is almost negligible in the mean. This indicates that the local SGS dynamics is ruled by different mechanisms from the global (mean) dynamics. This is confirmed by the r.m.s. values of the terms XV and XIII; although these two terms dominate the mean profiles, their r.m.s. values are low with $rms_{XV} = 0.296 \times 10^{-2}$ and $rms_{XIII} = 0.034 \times 10^{-2}$. The r.m.s. values show that the remaining two terms, XI (SGS pressure–velocity interactions) and XII (SGS viscous difussion) are negligible for the local SGS dynamics. The skewness factor of all the terms shows that their distribution is slightly asymmetric, except for the terms XIII and XV. This is expected since term XV averages into a high positive value, owing to the mean forward scatter, and term XIII into a mean negative value because it constitutes a sink of SGS kinetic energy. The flatness factor shows that all terms exhibit about the same level of intermittency except terms XV and XI. The intermittent nature of term XV was already discussed when dealing with its symmetric (VII) in (2.7). The fact that $F_{XV} \gg F_{XIII}$ can be easily understood; the sink term XIII is always negative

whereas the XV widely oscillates between positive (backscatter) and negative (forward scatter) values around a (negative) mean value. This clearly indicates the difference between the way energy arrives at the SGS level and the process by which it is finally dissipated by viscosity. The flatness suggests that the SGS viscous dissipation (term XIII), which is much less intermittent than all the other terms, acts as a background process present everywhere in the flow whereas the GS/SGS transfer (XV) constitutes a very intermittent process, sensitive to relatively rare flow events. It may be interesting to notice also that term XI, as happens with all viscous related terms in (2.7), acts through a highly intermittent processes. A final comment concerns the terms connected with the GS/SGS exchanges – terms XIV (= −VI) and XV (= −VII). Both their global (mean) and fluctuating (r.m.s.) values show that they belong to the most significant terms of the SGS dynamics. This was not the case for the GS dynamics since they were found to be relatively small compared to the other terms of (2.7). As expected, the SGS dynamics are therefore mainly commanded by the processes of receiving energy from the GS (term XV) and dissipating it by viscous dissipation (term XIII), while also diffusing (term XIV) and advecting this energy (term IX).

Let us turn now to the spatial localization of the dominant terms for the SGS dynamics. Visualizations of the spatial distribution of the SGS viscous dissipation (term XIII) are shown in figure 25. As previously stressed, this term is always negative since it corresponds to a sink of SGS kinetic energy. It can be seen that the higher (negative) values are located at the core of the flow vortices. This can also be verified with the joint PDF of XIII and the vorticity norm (see figure 23*a*) and with their correlation coefficient ($C_{(\Omega,XIII)} = -0.65$). Thus, the vortex core region of the coherent structures is a sink for both GS and SGS kinetic energy. The often assumed 'local equilibrium assumption' supposes that there is a local balance between the GS/SGS transfer and the SGS viscous dissipation,

$$2\nu\left(\left(\frac{\partial u_i}{\partial x_k}\frac{\partial u_i}{\partial x_k}\right)^{<} - \frac{\partial u_i^{<}}{\partial x_k}\frac{\partial u_i^{<}}{\partial x_k}\right) = 2\tau_{ik}S_{ik}^{<}. \tag{5.8}$$

This hypothesis constitutes the basic assumption of several SGS models such as, for instance, the Smagorinsky and the dynamic Smagorinsky models. As was seen above, and as expected, terms XV and XIII are in statistical equilibrium. However, the comparison of their spatial localization shown in figures 18 (term VII = −XV) and 25 (term XIII) clearly reveals that this equilibrium is not verified locally. The same was observed (not shown) for simulation DNS0 in the self-similar region, which shows that this lack of equilibrium is independent of the inlet noise amplitude. The SGS viscous dissipation acts within the core of the vortices, whereas the GS/SGS transfer takes place almost randomly in space and can be an energy source (forward-scatter) or an energy sink (backward-scatter) in (2.8). Thus, the energy transmitted to the SGS at a given location, is not going to be dissipated by molecular viscosity at that same location. The joint PDF of both terms is shown in figure 23(*b*). Their correlation coefficient is only $C_{(VII,XIII)} = 0.39$. Although there is some correlation between the terms, its relatively low level confirms the failure of the local equilibrium assumption. A possible explanation comes from the unexpected high local intensities (r.m.s.) of the term IX (SGS kinetic energy advection). A very high local SGS kinetic energy advection will transport energy received from the GS to another location before the viscosity has time to act. This hypothesis will be analysed below when discussing term IX.

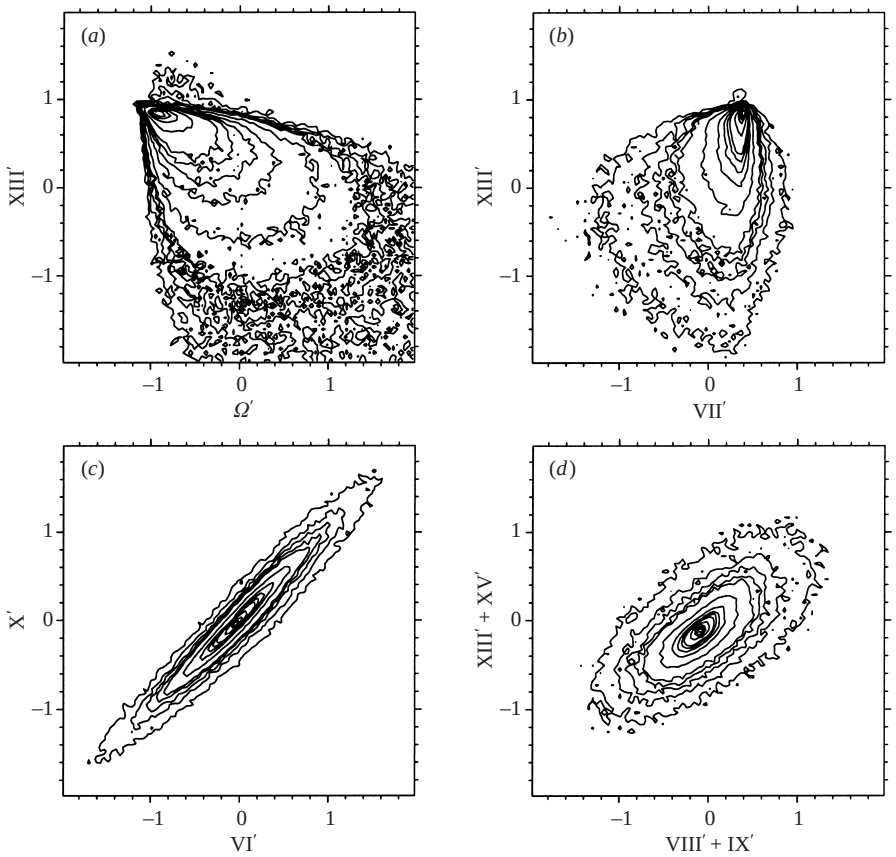

FIGURE 23. Several joint probability density functions (PDF) of terms from (2.7) and (2.8). For each joint PDF computation, all variables were removed from their mean values and non-dimensionalized by their respective variances. The PDFs were computed using the instantaneous fields from the DNS1 data bank at $x/h = 10$ and $y/h = 0.8$. DNS2 leads to similar results. For all the joint PDFs, 15, logarithmically placed isocontours were used. The isocontours are equally spaced and range from 2×10^{-3} to 1. The filter width was $\Delta_2 = 25\eta$. (*a*) Joint PDF of vorticity modulus and term XIII. (*b*) Joint PDF of terms VII and XIII. (*c*) Joint PDF of terms VI (= −XIV) and X. (*d*) Joint PDF of terms VIII + IX and XIII + XV.

Let us now turn in the SGS turbulent transport (term X). Visualizations of term X (not shown) show that it takes place mainly around the smaller vortices. It has a strong topological resemblance with term VI (= −XIV). This can be seen in the joint PDF of both terms shown in figure 23(*c*), and through their very high correlation coefficient $C_{(VI,X)} = +0.94$. Therefore, in (2.8), terms X and XIV are in local and statistical (seen above) equilibrium. However, it was observed that this balance is not verified within the transition region of the jet (not shown). Indeed, the small-scales turbulence has to reach a certain level for the SGS turbulent diffusion to start acting efficiently. This is important because it means that terms X and XIV, which otherwise could be neglected since they cancel each other out, have to remain in (2.8) when dealing with transitional flows.

The topology of term IX (SGS advection) will now be analysed. Visualizations of this term can be seen in figure 26. The picture clearly shows the existence of a clear connection between the vortex structures and the regions of high negative/positive

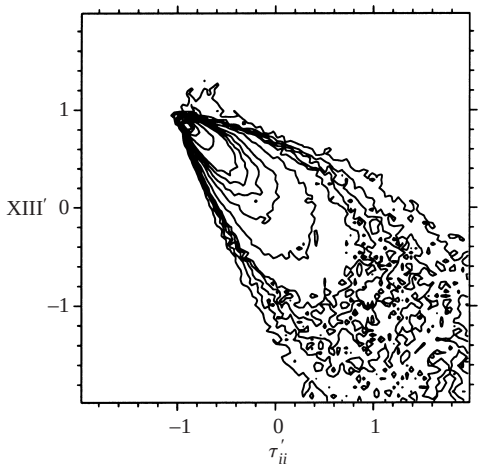

FIGURE 24. Joint PDF of subgrid-scale kinetic energy and term XIII from (2.8). For the joint PDF computation, both variables were removed from their mean values and non-dimensionalized by their respective variances. The PDF was computed using the instantaneous fields from the DNS1 data bank at $x/h = 10$ and $y/h = 0.8$. DNS2 leads to similar results. For this joint PDF, 15, logarithmically placed isocontours were used. The isocontours are equally spaced and range from 2×10^{-3} to 1. The filter width was $\Delta_2 = 25\eta$.

values of term IX. Notice that significant advection occurs preferentially at the periphery of the smallest most intense structures (as for term XIV $= -$VI already analysed), rather than within the large rollers (like terms II and III from (2.7)). Note that these small-scale intense structures can either be streamwise vortices or elongated vortices embedded within the core of the large rollers (see figures 3*b* and 4*b*). To characterize this correlation of IX with the coherent structures, the joint PDF (or the correlation coefficient) of this term and the vorticity modulus is not adapted since strong correlation takes place at the periphery of the vortices and not at their cores.

We now return to the problem of explaining why the 'local equilibrium assumption' fails. As stressed above, the very high local values (r.m.s.) of term IX found above, are a possible explanation to this. This can be demonstrated by considering a simplified form of the (2.8). From the previous discussion concerning the global and local intensities of the various terms of this equation, and since terms X and XIV cancel out (in the far-field region only), a good approximation of (2.8) can be obtained through,

$$\underbrace{\frac{\partial \tau_{ii}}{\partial t}}_{\text{VIII}} + \underbrace{\frac{\partial(\tau_{ii}u_k^<)}{\partial x_k}}_{\text{IX}} \approx 2\nu \underbrace{\left(\left(\frac{\partial u_i}{\partial x_k}\frac{\partial u_i}{\partial x_k}\right)^< - \frac{\partial u_i^<}{\partial x_k}\frac{\partial u_i^<}{\partial x_k}\right)}_{\text{XIII}} - 2\underbrace{\tau_{ik}S_{ik}^<}_{\text{XV}}. \tag{5.9}$$

In figure 23(*d*), the joint PDF of terms VIII + IX and XIII + XV shows there is a good local correlation between the two sides of the equation. The coefficient is $C_{(VIII+IX,XIII+XV)} = 0.57$. Given that terms XI and XII can be neglected and that terms X and XIV cancel out, this shows unambiguously that (5.9) is a good local approximation to the local SGS dynamics. This demonstrates that it is mainly SGS advection (term IX) and eventually local temporal variation of the SGS kinetic energy (term VIII) that compensates for the lack of local equilibrium between terms XIII and XV. This agrees with the findings of Borue & Orzag (1998), and illustrates one of the main difficulties of SGS modelling. It would be interesting to investigate the

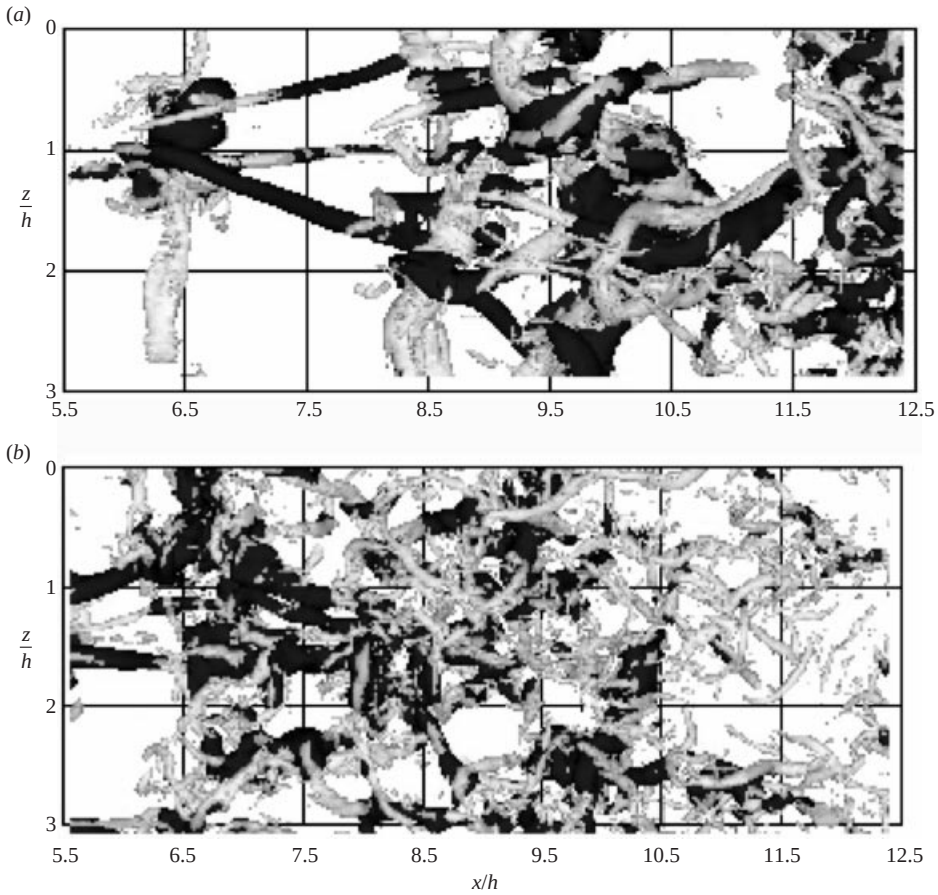

FIGURE 25. Visualizations of term XIII – SGS viscous dissipation (dark) and positive Q criterion (white grey) in the upper shear layer (top view) for DNS1 and DNS2. The figures correspond to the same instant as in figures 3(b) and 4(b), respectively, but the Q isosurfaces were made transparent (75% opacity) to help visualizations. The filter width is $\Delta_1 = 15\eta$. (a) Term XIII in DNS1. The threshold for term XIII is the following: dark corresponds to $-0.0175U_1^3/h$ and term XIII varies between $T_{min} = -0.45U_1^3/h$ and $T_{max} = 0$. (b) Term XIII in DNS2. The threshold for term XIII is the following: dark corresponds to $-0.04U_1^3/h$ and term XIII varies between $T_{min} = -0.5U_1^3/h$ and $T_{max} = 0$.

consequences of this (wrong) 'local equilibrium assumption' on the vortical structures resulting from Smagorinsky and dynamic Smagorinsky LES computations.

At this point, it is interesting to quote a remark made by a referee. For the SGS models that do not use the 'local equilibrium assumption', an equation for the subgrid-scale kinetic energy τ_{ii} transport is used instead. In general, the equation takes the form (Meneveau & O'Neil 1994),

$$\frac{\partial \tau_{ii}}{\partial t} + \frac{\partial (\tau_{ii} u_k^<)}{\partial x_k} = -2\tau_{ik} S_{ik}^< + \varepsilon_{xiii} + \frac{\partial Q_k}{\partial x_k}, \tag{5.10}$$

where Q_k represents the flux of τ_{ii} caused by the turbulence and ε_{xiii} represents the modelled viscous subgrid-scale kinetic energy dissipation. This term is supposed to model the effects described by term XIII in (2.8). This term is generally assumed to be proportional to the subgrid-scale kinetic energy,

$$\varepsilon_{xiii} \propto \tau_{ii}^{3/2}. \tag{5.11}$$

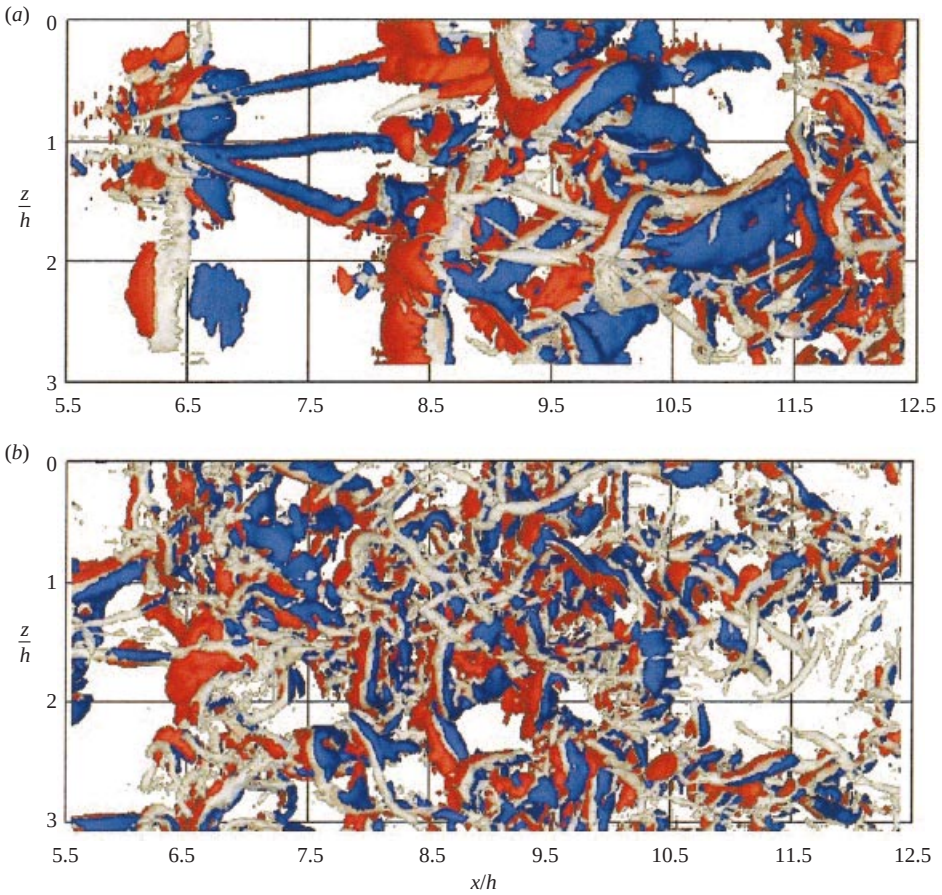

FIGURE 26. Visualizations of term IX – SGS kinetic energy advection (blue/red) and positive Q criterion (grey) in the upper shear layer (top view) for DNS1 and DNS2. The figures correspond to the same instant as in figures 3(b) and 4(b), respectively, but the Q isosurfaces were made transparent (75% opacity) to help visualizations. The filter width is $\Delta_1 = 15\eta$. (a) Term IX in DNS1. The threshold for term IX is the following: blue corresponds to $-0.1U_1^3/h$, red corresponds to $+0.1U_1^3/h$ and term IX varies between $T_{min} = -4.24U_1^3/h$ and $T_{max} = +4.57U_1^3/h$. (b) Term IX in DNS2. The threshold for term IX is the following: blue corresponds to $-0.175U_1^3/h$, red corresponds to $+0.175U_1^3/h$ and term VII varies between $T_{min} = -3.9U_1^3/h$ and $T_{max} = +3.7U_1^3/h$.

Using the data bank from DNS1 we found that the correlation between the subgrid-scale kinetic energy and the real term XIII is $C_{(\tau_{ii},XIII)} = -0.81$ (see their joint PDF in figure 24). Meneveau & O'Neil (1994) found it to be 0.6. As remarked by a referee, the fact that these values are higher than those assuming local equilibrium is an encouraging result for models based on τ_{ii} transport equations.

We now give a final note on terms XI (SGS pressure–velocity interactions) and XII (SGS viscous diffusion) which, as stated above, are negligible both for the mean and local SGS dynamics. Term XI, like the analogous term (III) of (2.7), exists mainly around the larger flow structures, but now the peaks of negative value are centred at the vortex cores which are surrounded by a region of high positive value (not shown). Next, term (XII) accounts for the viscous SGS diffusion and appears in part at the centre of the vortices (not shown), as indicated by the correlation coefficient between vorticity modulus and term XII which is $C_{(\Omega,XII)} = 0.47$.

Relevance	High	Medium	Negligible
Equation (2.7)	II, III	VI, VII	IV, V
Equation (2.8)	IX, X, XIV	XV, XIII	XI, XII

TABLE 6. Relevance of the several terms to (2.7) and (2.8). The criteria are based on the global (mean) and local (instantaneous) values of the terms compared to the other terms in the same equation. See text for details.

5.5. *Overview of interscale interactions: relevant terms and topological groups*

To summarize, a general overview is now given, concerning the most relevant terms and the topological groups for the GS and SGS kinetic energy dynamics in the turbulent plane jet.

Concerning the relevance (in terms of mean and local intensities) of the terms for the GS transport equation, (2.7), the most important terms are the GS advection (term II) and the GS pressure/velocity interactions (term III). Then come the GS/SGS diffusion (term VI) and the GS/SGS transfer (term VII). GS viscous diffusion and dissipation (terms IV and V) are negligible for the GS dynamics. For (2.8), the most important terms are SGS advection (term IX), SGS turbulent transport (term X), and GS/SGS diffusion (term XIV). In the far-field region (but not in the early stages of transition), terms X and XIV cancel out, and therefore the SGS advection (term IX) becomes the dominant term. At a second level of importance come the GS/SGS transfer (term XV) and SGS viscous dissipation (term XIII). Both SGS pressure/velocity interactions and SGS viscous diffusion (terms XI and XII) are negligible for the SGS dynamics in the far field of the turbulent plane jet. Table 6 summarizes these observations.

Our topological study revealed that the spatial localization of most of the terms of (2.7) and (2.8) is correlated with the various types of coherent structures, large Kelvin–Helmholtz vortices or smaller-scale elongated vortices (streamwise or in the Kelvin–Helmholtz core). It was seen above that both term IX and term X ($\approx$ XIV $= -$VI) appear mainly along the sides of the stronger smaller-scale vortices. It is therefore interesting to know how these two terms correlate. The terms are (anti) correlated as can be seen from their correlation coefficient which is $C_{(IX,X)} = -0.43$. Therefore, terms VI ($= -$XIV), IX and X seem to form a topological group, for which the main activity takes place around the smallest most intense vortices. The other group, associated with the periphery of the big rollers is formed by terms II and III (correlated with $C_{(II,III)} = +0.61$). To check out that these two groups are really distinct, we have computed their mutual correlation coefficient; for instance, we find $C_{(II,X)} = -0.24$. This clearly shows that the two topological groups, (II, III) and (VI $= -$XIV, IX, X) are separated. A third group is formed by the GS and SGS viscous dissipation (V, XIII) which are located at the core of the coherent vortices. Finally, no correlation exists between terms IV and VII ($= -$XV) and the presence of the coherent structures and neither terms XI or XII exhibit any correlation with each other or with other groups of more important terms i.e. group (II, III) or group (VI $= -$XIV, IX, X). The classification of the various terms into their topological groups is shown in table 7.

6. Conclusions

The main goal of this work was to understand how the GS/SGS interactions are affected by the presence of the vortical structures. This was performed by the

Topology group	A	B	C	D	E
Equation (2.7)	II, III	VI	V		IV, VII
Equation (2.8)		IX, X, XIV	XI, XIII	XII	XV

TABLE 7. Topology of terms from (2.7) and (2.8). Group A: higher values located around the (mainly large Kelvin–Helmholtz) vortex cores; group B: higher values located around the (mainly streamwise) vortex cores; group C: higher values located at the vortex cores; group D: negative peak at vortex cores and positive region around vortex cores. group E: no strong correlation observed with the presence of the coherent structures. Note that terms XIV and XV are the symmetric of terms VI and VII, respectively, and are therefore represented twice in the table.

application of a box filter to a plane-jet direct numerical simulation. The coherent structures, which were considered were the Kelvin–Helmholtz vortices and the longitudinal vortices which constitute the characteristic shear-flow structures associated with the energy containing and inertial range regions. The analysis of several one-point statistics, including PDFs, joint PDFs and the visualization of several instantaneous flow events allowed us to draw a clear picture of the role played by the coherent vortices in the complex GS/SGS interactions.

Even in the far field of an highly turbulent plane jet, most of the interactions between GS and SGS, either by diffusion or source terms, take place within or next to the cores of the flow vortical structures, and not randomly distributed in space. Therefore, the most important GS/SGS interactions are highly influenced by these local flow events. This agrees with the fact that most of the GS/SGS interactions are local (Domaradzki *et al.* 1993). GS kinetic energy advection (term II) and diffusion by GS pressure–velocity interactions (term III) are the most important terms for the evolution of the GS. Surprisingly, GS/SGS transfer (term VII $= -$XV) is not very well correlated with the far-field vortical structures in the turbulent plane jet. Moreover, its local and instantaneous values are one order of magnitude smaller than diffusion by GS/SGS diffusion (term VI $= -$XIV). This term turns out to play a major role in the GS and SGS dynamics. Therefore, its accurate modelling may be of primary importance in an LES aiming at a correct reproduction of the flow topology (vortical structures). We have separated the various terms into different categories depending on whether these occur mainly at the periphery of the large Kelvin–Helmholtz rollers, at the periphery of the smaller vortices or within the core of the coherent vortices. The last category is constituted by the terms which do not exhibit any clear correlation with the presence of the coherent structures. Roughly, three main categories appear: first, GS advection (term II) and the GS pressure/velocity interactions (term III) occur mainly next to the large Kelvin–Helmholtz rollers (group A). Secondly, the most intense values of SGS advection (term IX) and GS/SGS diffusion (term VI $= -$XIV) and turbulent transport (term X) occur around the smaller vortices (group B). Thirdly, the GS and SGS viscous dissipation (terms V and XIII) take place at the core of the coherent vortices (group C). Finally, it was shown that the 'local equilibrium' assumption is valid globally but not locally. The reason for this behaviour was shown to be the high local values of the SGS kinetic energy advection. This significant SGS advection, even at very small scales, illustrates the difficulties of SGS modelling. However, for SGS models based upon an SGS kinetic energy transport equation (Fureby *et al.* 1997; Davidson 1998), the present results show that in the far field of the plane jet, SGS diffusion is exactly balanced by the SGS turbulent transport. Therefore, these two

terms can be dropped out of the transport equation. The most important terms are then the SGS advection, SGS dissipation and SGS viscous dissipation. These three terms overshadow all others in (2.8), and a good SGS model cannot possibly fail in modelling them.

As a final comment, the present analysis illustrates once more that the dependence of the small scales on the large ones can be substantial even in a well-resolved LES. Since the types of vortex with which this study was concerned, appear in many free shear flows, the conclusions from the present work are extensible to free shear flows in general. Starting from the present analysis, future works should try to investigate how the different SGS models influence the shape of various (large-scale and inertial-range) vortices as well as their life time.

C. B. da S. is supported by the Portuguese government under scholarship PRAXIS XXI (5726/95). The simulations were carried out on an NEC SX5 machine from the Institut du Developpement et des Ressources en Informatique Scientifique (IDRIS).

REFERENCES

Akhavan, R., Ansari, A., Kang, S. & Mangiavacchi, N. 2000 Subgrid-scale interactions in a numerically simulated planar turbulent jet and implications for modelling. *J. Fluid Mech.* **408**, 83–120.

Balaras, E. & Piomelli, U. 1994 Subgrid-scale energy budgets in wall layer. *Bull. Am. Phys. Soc.* **39**, 1969.

Borue, V. & Orzag, S. A. 1998 Local energy flux and subgrid-scale statistics in three dimensional turbulence. *J. Fluid Mech.* **366**, 1–31.

Brancher, P., Chomax, J. M. & Huerre, P. 1993 Direct numerical simulations of round jets: vortex induction and side jets. *Phys. Fluids* **6**, 1768–1774.

Browne, L. W. B., Antonia, R. A., Rajagopalan, S. & Chambers, A. J. 1983 Interaction region of a two-dimensional turbulent plane jet in still air. In *Structure of Complex Turbulent Shear Flow* (ed. R. Dumas & L. Fulachier), pp. 411–419, IUTAM Symp. Marseille 1982, Springer.

Canuto, C., Hussaini, M. Y., Quarteroni, A. & Zang, T. A. 1987 *Spectral Methods in Fluid Dynamics*. Springer.

Cerutti, S., Meneveau, C. & Knio, O. M. 2000 Spectral and hyper eddy viscosity in high-Reynolds-number turbulence. *J. Fluid Mech.* **421**, 307–338.

Chua, L. P. & Lua, A. C. 1998 Measurements of a confined jet. *Phys. Fluids* **10**(12), 3137–3144.

Comte, P., Silvestrini, J. & Begou, P. 1998 Streamwise vortices in the large-eddy simulations of mixing layers. *Eur. J. Mech.* B *Fluids* **17**, 615–637.

Davidson, L. 1998 Large eddy simulation: a dynamic one equation subgrid model for three-dimensional recirculating flow. In *Proc. 11th Turbulent Shear Flows, Grenoble*, pp. 26:1–26:6.

Domaradzki, J. A., Liu, W. & Brachet, M. E. 1993 An analysis of subgrid-scale interactions in numerically simulated isotropic turbulence. *Phys. Fluids* **5**, 1747–1759.

Domaradzki, J. A., Liu, W., Hartel, C. & Kleiser, L. 1994 Energy transfer in numerically simulated wall-bounded flows. *Phys. Fluids* **6**, 1583–1599.

Domaradzki, J. A. & Rogallo, R. 1990 Local energy transfer and nonlocal interactions in homogeneous, isotropic turbulence. *Phys. Fluids* **2**, 413–426.

Dubief, Y. & Delcayre, F. 2000 On coherent-vortex identification in turbulence. *J. Turbulence* **1**(011).

Fureby, C., Tabor, G., Weller, H. G. & Gosman, A. D. 1997 Differential subgrid stress models in large eddy simulations. *Phys. Fluids* **9**, 3578–3580.

Gonze, M. A. 1993 Simulation numérique des sillages en transition à la turbulence. PhD thesis, INPG, Grenoble.

Guerts, B. J., de Bruin, I. C. C. & Sarkar, S. 2000 Rapid and slow contribuitions to the turbulent stress tensor and inverse modeling in a turbulent mixing layer. In *Advances in Turbulence VIII* (ed. C. Dopazo), pp. 539–542. CIMNE, Barcelona.

Gutmark, E. & Wygnansky, I. 1976 The planar turbulent jet. *J. Fluid Mech.* **73**, 465–495.

Hartel, C. & Kleiser, L. 1998 Analysis and modelling of subgrid-scale motions in near wall turbulence. *J. Fluid Mech.* **356**, 327–352.

Horiuti, K. 1995 Subgrid-scale energy production mechanism in large-eddy simulations. *Proc. Intl Symp. Math. Modelling of Turbulent Flows, Tokyo*, pp. 164–169.

Horiuti, K. 1996 Assessment of the subgrid-scale models at low and high Reynolds numbers. *Annu. Res. Briefs.* Center for Turbulence Research.

Horiuti, K. 1997 Backward scatter of subgrid-scale energy in wall-bounded and free shear turbulence. *J. Phys. Soc. Japan* **66**, 91–107.

Horiuti, K. 2000 Assessement of subgrid-scale models in dissipative vortical structures. In *Advances in Turbulence VIII* (ed. C. Dopazo), pp. 519–522. CIMNE, Barcelona.

Hunt, J. C. R., Wray, A. A. & Moin, P. 1988 Eddies, stream, and convergence zones in turbulent flows. *Rep. CTR-S88.* Center for Turbulence Research.

Hussain, A. K. M. F. & Clark, A. R. 1977 Upstream influence on the near field of a plane turbulent jet. *Phys. Fluids* **20**, 1416–1426.

Hussain, A. K. M. F. 1983 Coherent structures – reality and myth. *Phys. Fluids* **26**, 2816–2850.

Hussain, A. K. M. F. 1986 Coherent structures and turbulence. *J. Fluid Mech.* **173**, 303–356.

Jiménez, J. 1999 The physics of wall turbulence. *Physica* A **263**, 253–262.

Jiménez, J., Wray, A. A., Saffman, P. G. & Rogallo, R. S. 1993 The structure of intense vorticity in isotropic turbulence. *J. Fluid Mech.* **225**, 65–90.

Kawahara, G., Kida, S., Yanase, S. & Tanaka, S. 2000 Energy dissipation in spiral vortex layers wrapped around a diffusing straight vortex tube. In *Advances in Turbulence VIII* (ed. C. Dopazo), pp. 733–736. CIMNE, Barcelona.

Kerr, R. M., Domaradzki, J. A. & Barbier, G. 1996 Small-scale properties of nonlinear interactions and subgrid-scale energy transfer in isotropic turbulence. *Phys. Fluids* **8**, 197–208.

Kim, J. & Moin, P. 1985 Application of a fractional-step method to incompressible Navier–Stokes equations. *J. Comput. Phys.* **59**, 308–323.

Kolmogorov, A. N. 1941 On degeneration of isotropic turbulence in an incompressible viscous liquid. *Dokl. Akad. Nauk. SSSR* **31**, 538–541.

Le, H. & Moin, P. 1991 An improvement of fractional-step methods for the incompressible Navier–Stokes equations. *J. Comput. Phys.* **92**, 369–379.

Le Ribault, C., Sarkar, S. & Stanley, S. A. 1999 Large eddy simulation of a plane jet. *Phys. Fluids* **11**, 3069–3083.

Lele, S. K. 1992 Compact finite difference schemes with spectral-like resolution. *J. Comput. Phys.* **103**, 16–42.

Lesieur, M. 1997 *Turbulence in Fluids*, 3rd edn. Kluwer.

Lesieur, M. & Métais, O. 1996 New trends in large-eddy simulations of turbulence. *Annu. Rev. Fluid Mech.* **28**, 45–82.

Lin, C.-L. 1999 Near-grid-scale energy transfer and coherent structures in the convective planetary boundary layer. *Phys. Fluids* **11**, 3482–3494.

Liu, S., Katz, J. & Meneveau, C. 1999 Evolution and modelling of subgrid scales during rapid straining of turbulence. *J. Fluid Mech.* **387**, 281–320.

Liu, S., Meneveau, C. & Katz, J. 1994 On the properties of similarity subgrid-scale models as deduced from measurements in a turbulent jet. *J. Fluid Mech.* **275**, 83–119.

Meneveau, C. & Katz, J. 1999 Conditional subgrid force and dissipation in locally isotropic and rapidly strained turbulence. *Phys. Fluids* **11**, 2317–2329.

Meneveau, C. & Katz, J. 2000 Scale-invariance and turbulence models for large-eddy simulation. *Annu. Rev. Fluid Mech.* **32**, 1–32.

Meneveau, C. & O'Neil, J. 1994 Scaling laws of the dissipation rate of turbulent subgrid-scale kinetic energy. *Phys. Rev.* E **49**, 2866–2874.

Métais, O. & Herring, J. R. 1989 Numerical simulations of freely evolving turbulence in stably stratified fluids. *J. Fluid Mech.* **202**, 117–148.

Métais, O. & Lesieur, M. 1992 Spectral large-eddy simulation of isotropic and stably stratified turbulence. *J. Fluid Mech.* **239**, 157–194.

Moin, P. & Mahesh, K. 1998 Direct numerical simulation: a tool in turbulence research. *Annu. Rev. Fluid Mech.* **30**, 539–579.

Monin, A. S. & Yaglom, A. M. 1975 *Statistical Fluid Mechanics: Mechanics of Turbulence*, vol. 2. MIT Press, Cambridge, MA.

Monkewitz, P. A. & Huerre, P. 1982 Influence of the velocity ratio on the spatial instability of mixing layers. *Phys. Fluids* **25**, 1137–1143.

Moffatt, H. K., Kida, S. & Ohkitani, K. 1994 Stretched vortices – the sinews of turbulence; large-Reynolds-number asymptotics. *J. Fluid Mech.* **259**, 241–264.

O'Neil, J. & Meneveau, C. 1997 Subgrid-scale stresses and their modelling in a turbulent plane wake. *J. Fluid Mech.* **349**, 253–293.

Orlansky, I. 1976 A simple boundary condition for unbounded hyperbolic flows. *J. Comput. Phys.* **21**, 251–269.

Piomelli, U., Cabot, W. H., Moin, P. & Lee, S. 1991 Subgrid-scale backscatter in turbulent and transitional flows. *Phys. Fluids* **3**, 1766–1771.

Piomelli, U. & Chasnov, J. R. 1996 *Large Eddy Simulations: Theory and Applications* (ed. M. Hallback, D. S. Henningson, A. V. Jhoannson & P. H. Alfredssoon). Kluwer, 1996.

Piomelli, U., Coleman, G. & Kim, J. 1997 On the effects of nonequilibrium on the subgrid-scale stresses. *Phys. Fluids* **9**, 2740–2748.

Piomelli, U., Yu, Y. & Adrian, R. J. 1996 Subgrid-scale energy transfer and near-wall turbulence structure. *Phys. Fluids* **8**, 215–224.

Ramprian, B. R. & Chandrasekhara, M. S. 1985 LDA measurements in plane turbulent jets. *Trans. ASME* I: *J. Fluids Engng* **107**, 264–271.

Rogallo, R. S. & Moin, P. 1984 Numerical simulation of turbulent flows. *Annu. Rev. Fluid Mech.* **16**, 99–137.

Schumann, U. 1975 Subgrid-scale model for finite difference simulations of turbulent flows in plane channels and annuli. *J. Comput. Phys.* **18**, 376–404.

Silvestrini, J. 1996 Simulation des grandes échelles des zones de mélange; application à la propulsion solide des lanceurs spatiaux. PhD thesis, INPG, Grenoble.

Smagorinsky, J. 1963 General circulation experiments with the primitive equations. *Mon. Weather Rev.* **91**, 99–164.

Stanley, S. A. & Sarkar, S. 2000 Influence of nozzle conditions and discrete forcing on turbulent planar jets. *AIAA J.* **38**, 1615–1623.

Stanley, S. A., Sarkar, S. & Mellado, J. P. 2002 A study of the flowfield evolution and mixing in a planar turbulent jet using direct numerical simulation. *J. Fluid Mech.* **450**, 377–407.

Tennekes, H. & Lumley, J. L. 1972 *A First Course in Turbulence*. MIT Press, Cambridge, MA.

Thomas, F. O. & Chu, H. C. 1989 An experimental investigation of the transition of the planar jet: subharmonic suppression and upstream feedback. *Phys. Fluids* **1**, 1566–1587.

Thomas, F. O. & Goldschmidt, V. W. 1986 Structural characteristics of a developing turbulent plane jet. *J. Fluid Mech.* **163**, 227–256.

Thomas, F. O. & Prakash, K. M. K. 1991 An investigation of the natural transition of an untuned planar jet. *Phys. Fluids* **3**, 90–105.

Tsubokura, M., Kobayashi, T. & Taniguchi, N. 2000 Subgrid scale modeling of turbulence considering the effect of external force. *Proc. Turbulent Shear Flow Phenomena*, pp. 875–880.

Vincent, A. & Meneguzzi, M. 1991 The spatial structure and statistical properties of homogeneous turbulence. *J. Fluid Mech.* **225**, 1–20.

Vreman, B., Geurts, B. & Kuerten, H. 1997 Large eddy simulation of the turbulent mixing layer. *J. Fluid Mech.* **339**, 357–390.

Williamson, J. H. 1980 Low-Storage Runge–Kutta schemes. *J. Comp. Phys.* **35**, 48–56.

Zeman, O. 1995 The persistence of trailing vortices: a modelling study. *Phys. Fluids* **7**, 135–143.